

1 **A model for interpreting the deformation mechanism of reservoir landslides in the**
2 **Three Gorges Reservoir area, China**

3 Zongxing Zou¹, Huiming Tang¹, Robert E. Criss², Xinli Hu³, Chengren Xiong¹, Qiong
4 Wu³, Yi Yuan⁴

5 ¹Three Gorges Research Center for geo-hazards, China University of Geosciences, Wuhan, 430074,
6 China

7 ²Department of Earth and Planetary Sciences, Washington University, One Brookings Drive, Saint
8 Louis, United States

9 ³Faculty of Engineering, China University of Geosciences, Wuhan, 430074, China

10 ⁴Department of Land and Resources of Hubei Province, Wuhan, 430074, China

11 *Correspondence author: Huiming Tang (tanghm@cug.edu.cn)*

12

13 **Abstract.** Landslides whose slide surface is gentle near the toe and relatively steep in the middle
14 and rear part are common in the Three Gorges Reservoir area, China. The mass that overlies the
15 steep part of the slide surface is termed the “driving section” and that which overlies the gentle part
16 of the slide surface is termed the “resisting section”. A driving-resisting model is presented to
17 elucidate the deformation mechanism of reservoir landslides of this type, as exemplified by Shuping
18 landslide. More than 13 years of field observations that include rainfall, reservoir level and
19 deformation show that the displacement velocity of Shuping landslide depends strongly on the
20 reservoir level but only slightly on rainfall. Seepage modelling shows that the landslide was
21 destabilized shortly after the reservoir was first impounded to 135 m, which initiated a period of
22 steady deformation from 2003 to 2006 that was driven by buoyancy forces on the resisting section.
23 Cyclical water-level fluctuations in subsequent years also affected slope stability, with annual
24 “jumps” in displacement coinciding with drawdown periods that produce outward seepage forces. In
25 contrast, the inward seepage force that results from rising reservoir levels stabilizes the slope, as
26 indicated by decreased displacement velocity. Corrective transfer of earth mass from the driving
27 section to the resisting section successfully reduced the deformation of Shuping landslide, and is a
28 feasible treatment for huge reservoir landslides in similar geological settings.

29 **Keywords:** Three Gorges Reservoir, Reservoir landslide, Water level fluctuation, Deformation
30 mechanism, Shuping landslide

31

32 **1 Introduction**

33 Reservoir landslides attract wide attention as they can cause huge surge waves and other
34 disastrous consequences (Huang et al., 2017; Wen et al., 2017; Froude and Petley, 2018). The surge
35 wave produced by the 1963 Vajont landslide in Italy destroyed Longarone village and caused nearly
36 2,000 fatalities (Paronuzzi and Bolla, 2012). A similar surge associated with the 2003 Qianjiangping
37 landslide, which slipped shortly after the Three Gorges Reservoir (TGR) in China was first
38 impounded, capsized 22 fishing boats and took 24 lives (Xiao et al., 2007; Tang et al., 2019).
39 **However, reinforcement structures are costly and difficult to construct, and thus many huge reservoir**
40 **landslides have not been treated (Wang and Xu, 2013).** Many remain in a state of continuous
41 deformation, such that cumulative monitored displacements of several meters are now documented at
42 the Huangtupo (Tang et al., 2015; Zou et al., 2020; Dumperth et al., 2016), Outang (Yin et al., 2016),
43 and Baishuihe (Li et al., 2010; Du et al., 2013) landslides. Additional study of the deformation and
44 failure mechanisms, and risk reduction strategies of these huge reservoir landslides is of great
45 significance.

46 Most research on the deformation or failure mechanism of reservoir landslides involves
47 numerical modelling, physical model testing, or field observation. Many numerical simulations have
48 studied how landslide geometry, material permeability, variation rate of water level and pressure
49 variation influence the stability of reservoir landslides (Rinaldi and Casagli, 1999; Lane and Griffiths,
50 2000; Liao et al., 2005; Cojean and Cai, 2011; Song et al., 2015). Both small-scale (Junfeng et al.,
51 2004; Hu et al., 2005; Miao et al., 2018) and large-scale physical model experiments (Jia et al., 2009)

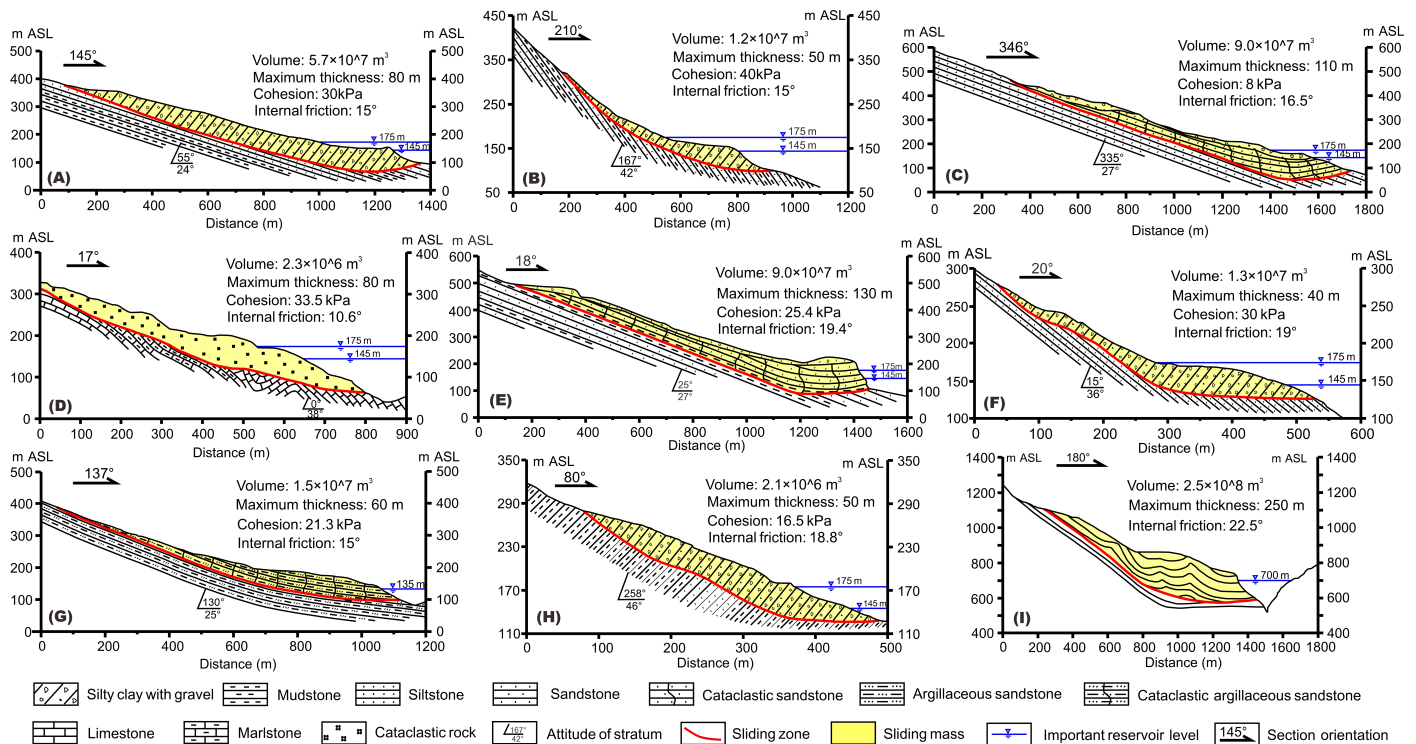
52 have been conducted to investigate the deformation features of reservoir landslides related to water
53 level change. Casagli et al. (1999) and Rinaldi et al. (2004) monitored the pore water pressure in
54 riverbanks to determine its effect on bank stability.

55 Since the impoundment of TGR, monitoring systems have been installed on or within many
56 reservoir landslides (Ren et al., 2015; Huang et al., 2017; Song et al., 2018; Wu et al., 2019), which
57 provide valuable data for the study of their deformation features. Many studies show that reservoir
58 water level variations and rainfall are the most critical factors that govern the stability and
59 displacement velocities of reservoir landslides in TGR (Li et al., 2010; Tang et al., 2015; Ma et al.,
60 2016; Wang et al., 2014). These phenomena are more obvious in the landslides with lower
61 permeability and in the situations of rapid drawdown and heavy rainfall. In the low permeability
62 landslide, the groundwater is not easy to be discharged from the slope in the process of rapid
63 drawdown and rainfall infiltration, which results in the formation of pressure difference between
64 inside and outside of the landslide and reduces the stability of the landslide. However, the effects of
65 rainfall and reservoir level are difficult to distinguish because the period of TGR drawdown is
66 managed to coincide with the rainy season. Detailed deformation studies that incorporate long-term
67 continuous monitoring data are needed to quantify how periodic water-level variations affect
68 reservoir landslides. Moreover, the evolutionary trend of these deforming landslides and feasible
69 treatments for these huge reservoir landslides are rarely studied.

70 Many researchers have noticed that different parts of the slide mass play different role in the
71 landslide stability. Terzaghi and Peck (1967), Sultan and Seed (1967) presented wedge method for
72 analyzing landslides consisting of an active driving wedge and resisting block. Hutchinson (1984)

73 presented an "influence-line" approach for assessing effectiveness of cuts and fills in stabilizing
74 slopes. Baum and Fleming (1991) derived expressions for the boundary between driving and
75 resisting elements of landslides for a shallow landslide. Iverson (1986), McKean and Roering (2004),
76 Guerriero et al. (2014), Prokesova et al. (2014), and Handwerger et al. (2015) have further explored
77 the influence of slip surface and landslide geometry on landslide deformation, force distribution and
78 landslide dynamics. These works provide a new perspective for the studying reservoir landslides.

79 This study presents a model combined with seepage simulations to elucidate how reservoir
80 landslides deform, using the Shuping landslide as an example. The new environmental and
81 deformation data provided here extend the observational period for this landslide to more than 13
82 years, and include results that confirm the effectiveness of a control strategy that have been
83 implemented.



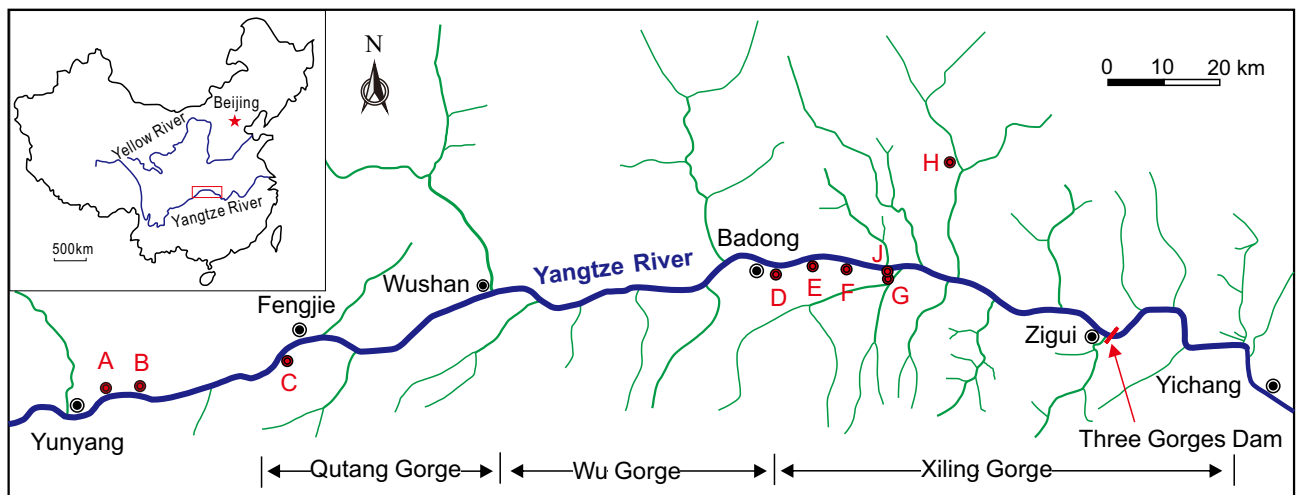
84

85 **Fig. 1** Geological profiles for typical reservoir landslides, all in the TGR except Vajont in Italy (I).
 86 (A) Jiuxianping landslide (Wang, 2013); (B) Xicheng landslide (Song, 2011); (C) Outang landslide
 87 (Yin et al., 2016); (D) No.1 riverside slump of Huangtupo landslide (Wang et al., 2014); (E)
 88 Muyubao landslide (Lu, 2012); (F) Baishuihe landslide (Lu, 2012); (G) Qiangjiangping landslide
 89 (Xiao et al., 2007); (H) Ganjuyuan landslide (Qin, 2011); (I) Vajont landslide, the world famous
 90 reservoir-induced landslide in Italy (Paronuzzi and Bolla, 2012). See Fig. 2 for locations.

91 2 A geomechanical model for reservoir-induced landslide

92 2.1 Typical reservoir-induced landslides in the Three Gorges Reservoir

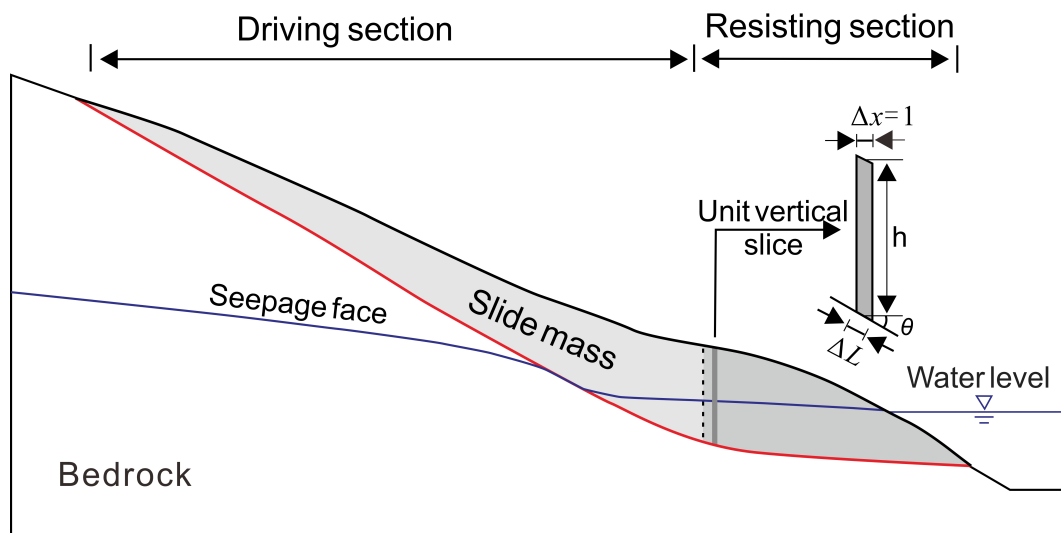
93 Figure 1 and Fig. 2 summarize the reservoir landslides of most concern in the TGR plus the
94 world famous Vajont landslide. These landslides have many common features. First, all these
95 landslides have large volumes, ranging from millions of cubic meters to tens of millions of cubic
96 meters, and all are difficult to reinforce by conventional structures such anti-slide pile, retaining wall
97 etc. Second, the front part of the slide mass is always thicker than the rear part, with a maximum
98 thickness from 40 m to over 100 m. Another important feature of these profiles (Fig. 1) is that the
99 slope of the slide surface decreases gradually from the rear to the front and may become horizontal
100 or even anti-dip in the front. Last, these landslides were reactivated after the reservoir impoundment,
101 with large observed deformations indicating their metastable situation. All these features are relevant
102 to the deformation behavior of reservoir landslides, as discussed below.



104 **Fig. 2** Location map for important landslides in TGR. Jiuxianping landslide (A); Xicheng landslide
105 (B); Outang landslide (C); Huangtupo landslide (D); Muyubao landslide (E); Baishuihe landslide (F);
106 Qiangjiangping landslide (G); Ganjuyuan landslide (H); Shuping landslide (J), Case study.

107 **2.2 Driving-resisting model**

108 Due to the relatively high slope of the slide surface in the middle and rear part, the slide force
109 exceeds the resistance force on the proximal slide surface, producing extra thrust on the lower-front
110 slide mass. Consequently, the rear-upper is termed the “driving section” (Fig. 3). In contrast, the
111 potential slide surface underlying the lower-front part of the slide mass provides more resistance due
112 to the relatively gentle slide surface slope and greater thickness of the slide mass. The lower-front
113 part of the slide mass is termed the “resisting section” (Fig. 3), as it provides main resistance force
114 for the whole slide mass, thereby playing a critical role in landslide stability (Tang et al., 2015).



115

116

Fig. 3 Driving-resisting model for reservoir landslide

117 The resisting section is defined as the lower-front part of the slide mass, where each unit vertical
118 slice (Fig. 3) can be self-stabilized under its self-weight. According to the limit equilibrium method
119 and the definition of the resisting section, the sliding force of each vertical slice is the component of
120 its gravitational force along the slide surface, which cannot exceed the shear resistance provided by
121 the base. The special position where the sliding force of the vertical slice equals the resistance force

122 provided by the slide surface is regarded as the boundary between the driving and resisting sections.
 123 In the unit vertical slice of resisting section, the difference between the forces on the two vertical
 124 sides is very tiny because the width of the unit vertical slice is very small, and the slide surface
 125 underlying the lower-front part of the slide mass is relatively gentle; so the interslice forces were
 126 ignored for the convenience of analysis. Force balance along the sliding direction for this special
 127 vertical slice can be written as

$$128 \quad w \sin \theta_1 = w \cos \theta_1 \tan \varphi + c \Delta L \quad (1)$$

129 where w is the weight of the unit vertical slice; θ_1 is the slope angle of the slide surface at the
 130 boundary between the driving and resisting sections; ΔL is the length of the slice base (see Fig. 3);
 131 and c and φ are the cohesion and internal friction angle of the slide surface, respectively.

132 The weight of the slice $w = \gamma h \Delta x$, where γ is the unit weight of the slide mass, h is the vertical
 133 distance from the center of the base of the slice to the ground surface, Δx is the unit width of the slice,
 134 and $\Delta L = \Delta x / \cos \theta_1$ (Fig. 3). Thus Eq. (1) can be rewritten as

$$135 \quad \tan \theta_1 = f + k / \cos^2 \theta_1 \quad (2)$$

136 where $f = \tan \varphi$, $k = c / \gamma h$.

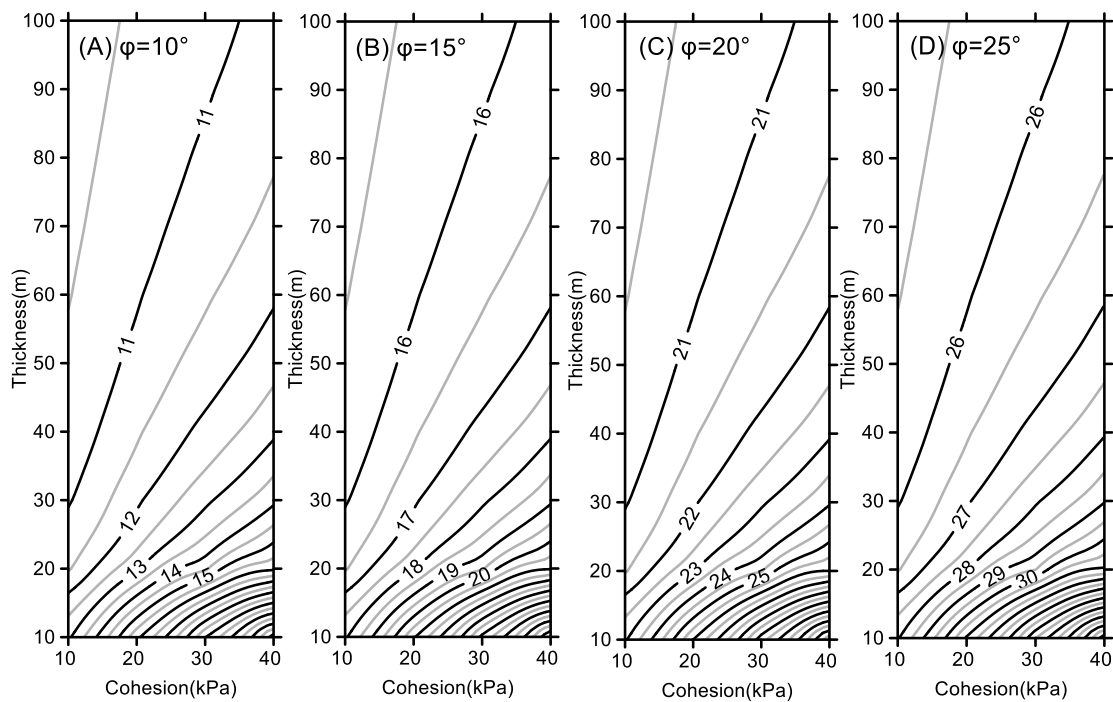
137 The solution to Eq. (2) provides the slope angle θ_1 of the slide surface:

$$138 \quad \theta_1 = 0.5 \arcsin T \quad (3)$$

$$139 \quad \text{where } T = \frac{(2k + f) + \sqrt{(2k + f)^2 - 4k(k + f)(1 + f^2)}}{1 + f^2}$$

140 According to the range of the shear strength parameters of the slip zone soil presented in
 141 Engineering Geology Manual (Chang et al., 2007), empirical values for the cohesion of the slide

142 surface is commonly less than 40 kPa, while the internal friction angle of the slide surface commonly
 143 varies between 10° and 25° , and the unit weight of the soil is typically about 20 kN/m^3 . In order to
 144 further elucidate the effect of various parameters on the length of the resisting section, contour maps
 145 of θ_1 under different shear strength parameters c and ϕ and the thickness of the slide mass h are
 146 plotted (Fig. 4), as derived from Eq. (3).



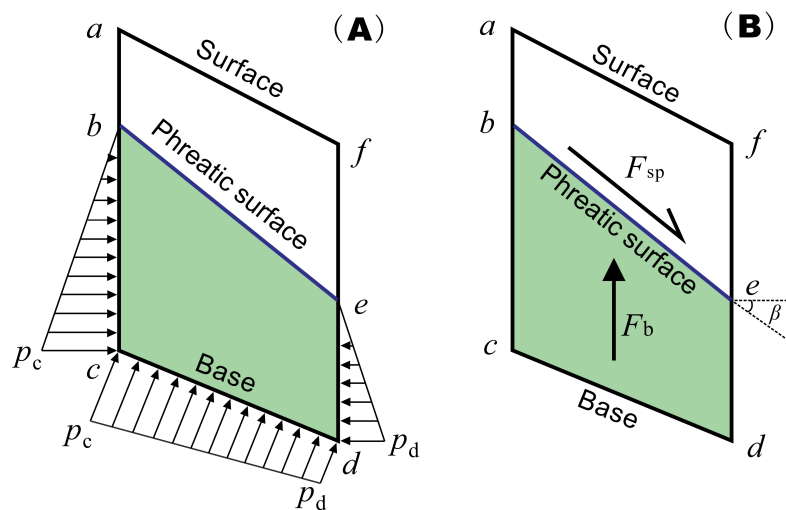
147
 148 **Fig. 4** Coutour maps for the slope angle θ_1 of slide surface that denotes the boundary between the
 149 driving and resisting sections under various shear strength parameters and slide mass thickness.

150 Figure 4 shows that θ_1 increases as the internal friction angle ϕ increases; however, by
 151 comparison of the pattern and the values of the contour in the four sub-figures, the difference
 152 between θ_1 and ϕ has little relationship to ϕ . Due to the effect of cohesion, θ_1 is always larger than ϕ
 153 as shown in Fig. 4. As the cohesion c decreases, the difference between θ_1 and ϕ decreases, and for
 154 cohesionless material with $c=0$, θ_1 is equal to ϕ . Fig. 4 also shows that when the thickness of the slide

155 mass reaches about 40 m, the difference between θ_1 and φ is very small (less than 3°), which
 156 becomes even less as the thickness increases. These results indicate that for the thick slide mass (up
 157 to 40 m), the boundary between the resisting and driving sections can be approximated as the
 158 position where the slope angle θ_1 equals the internal friction angle φ .

159 2.3 Effect of water force on the resisting and driving sections

160 The impacts of the water level change on the reservoir slope stability can be quantified by
 161 analyzing the changes in water force on the slope. Lambe and Whitman (2008) have demonstrated
 162 that the water forces acting on an element of the slope can be equivalently expressed by either the
 163 ambient pore-water pressure (Fig. 5A) or by seepage and buoyancy forces (Fig. 5B). The latter form,
 164 i.e., seepage and buoyancy forces, are employed here to clarify the mechanical mechanism of water
 165 force on the reservoir bank.



166
 167 **Fig. 5** Two equivalent ways to display the water force acting on a slice of the slide mass. (A)
 168 expressed by pore-water pressure; (B) expressed by the seepage force F_{sp} and the buoyancy force F_b .

169 The seepage force (F_{sp}) represents the frictional drag of water flowing through voids that is

170 proportional to the hydraulic gradient and acts in the direction of flow (Lambe and Whitman, 2008).

171 It can be expressed as

$$172 \quad F_{sp} = \gamma_w i V \quad (4)$$

173 where γ_w is the unit weight of water; i is the hydraulic gradient and equals $\sin\beta$ where β is the slope
174 angle of the phreatic surface; V is the submerged volume of the analyzed element as the trapezoid
175 area enclosed by points bcd e in Fig. 5.

176 When the groundwater flows outwards as occurs during reservoir level drops, the corresponding
177 outward seepage force decreases the slope stability. In contrast, the seepage force will be directed
178 inward during reservoir level rise, increasing slope stability.

179 The buoyancy force (F_b) of the water exerted on the element can be expressed as

$$180 \quad F_b = \gamma_w V \quad (5)$$

181 The factor of safety (Fos) used to quantify the slope stability can be defined as the ratio of the
182 shear strength (resistance, F_r) along the potential failure surface to the sliding force (F_s) by the
183 Mohr-Coulomb failure criterion (Wang et al., 2014):

$$184 \quad Fos = \frac{F_r}{F_s} = \frac{\sum_{j=1}^n [c\Delta L_j + N_j \tan \varphi]}{\sum_{j=1}^n w_j \sin \theta_j} \quad (6)$$

185 where n is the total number of slices; N is the normal force on the base of each slice, and the other
186 symbols are as above. Suppose that the variation of the effective slide mass weight in a slice is Δw ,
187 due to the change of buoyancy force, which thereby modifies the resistance and sliding forces by ΔF_r
188 and ΔF_s respectively. The corresponding change of the factor of safety ΔFos is

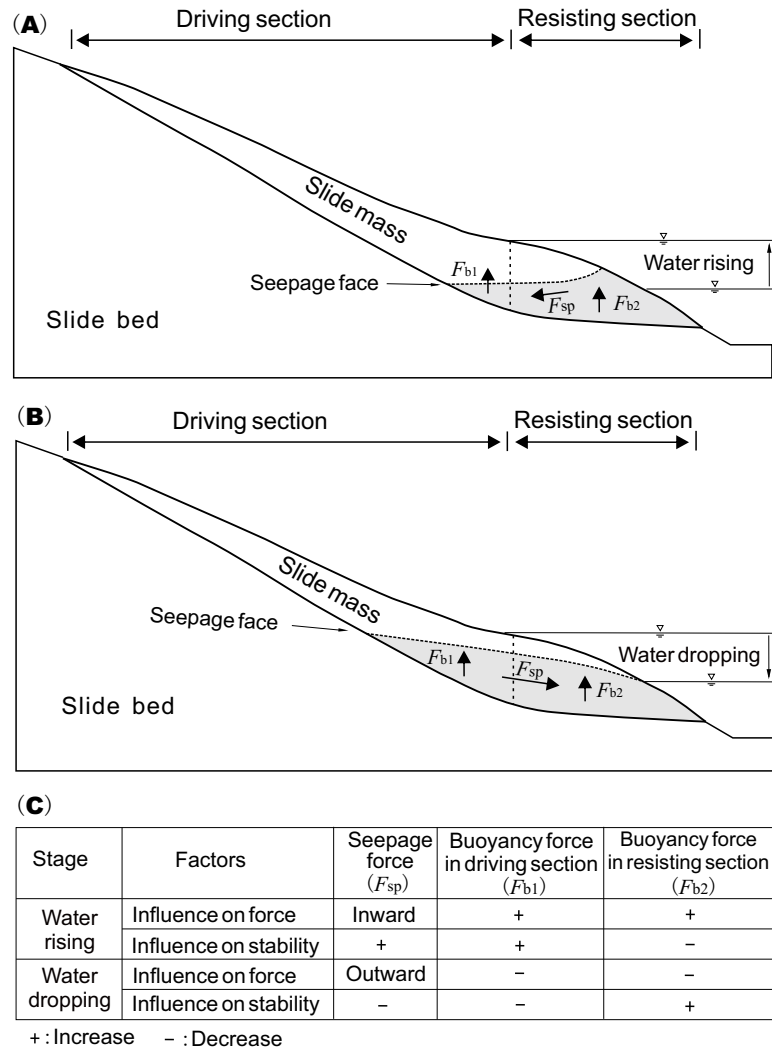
189
$$\Delta Fos = \frac{F_r + \Delta F_r}{F_s + \Delta F_s} - \frac{F_r}{F_s} = \frac{\Delta F_r * F_s}{(F_s + \Delta F_s) F_s} \left(1 - \frac{Fos}{\Delta F_r / \Delta F_s} \right) \quad (7)$$

190 The ratio of ΔF_r to ΔF_s for a vertical slice due to the change of its effective weight Δw is
 191 approximately

192
$$\frac{\Delta F_r}{\Delta F_s} = \frac{\Delta w \cos \theta \tan \varphi}{\Delta w \sin \theta} = \frac{\tan \varphi}{\tan \theta} \quad (8)$$

193 Suppose that $\theta_2 = \arctan\left(\frac{\tan \varphi}{Fos}\right)$, where the change of the vertical slice weight has no influence
 194 on the current stability ($\Delta Fos = 0$). If $\theta < \theta_2$ and $\Delta w > 0$, then $\Delta Fos > 0$, indicating that increase of the
 195 weight of lower-front part of the slide mass where its slope angle of the slide surface θ is less than θ_2
 196 will improve the stability of the whole slide mass; conversely, decrease of the weight of the
 197 lower-front part would decrease stability. In contrast, the upper-rear part has a contrary tendency. As
 198 mentioned above, continuously deformed reservoir landslides are metastable and their corresponding
 199 Fos is around 1; hence $\theta_2 \approx \varphi$. Consequently, in the cases that reservoir landslide is under metastable
 200 state and has a thickness up to 40 m, $\theta_1 \approx \theta_2 \approx \varphi$, the resisting section and driving section have the same
 201 mechanical behavior as described above. Either an increase in the weight of the resisting section or a
 202 decrease in the weight of the driving section will improve the stability of the slope and vice versa.

203 In summary, the effect of ground water on the slope or landslide stability can be resolved into a
 204 seepage force and a buoyancy force. The effect of the seepage force on slope stability depends on the
 205 direction and magnitude of flow. Buoyant forces change the effective weight of the slide mass and
 206 have contrary effect on the resisting and driving sections. On the basis of these rules, the mechanical
 207 mechanism for reservoir-induced landslide can be illustrated as Fig. 6.



208

209 **Fig. 6** Mechanical mechanism for reservoir-induced landslide. (A) water level rise; (B) water level
 210 drop; (C) effects of various mechanisms on the landslide stability during water level rise and drop.

211 **3 Shuping landslide**

212 Shuping landslide is located in Shazhenxi Town, Zigui County, Hubei Province, on the south
 213 bank of the Yangtze River, 47 km upstream from the Three Gorges dam (Fig. 2). After the first
 214 impoundment of the reservoir in 2003, serious deformation was observed that endangered 580
 215 inhabitants and navigation on the Yangtze River (Wang et al., 2007). Previous studies of the Shuping
 216 landslide utilized GPS extensometers (Wang et al., 2007), or field surveys (Lu et al., 2014) to clarify

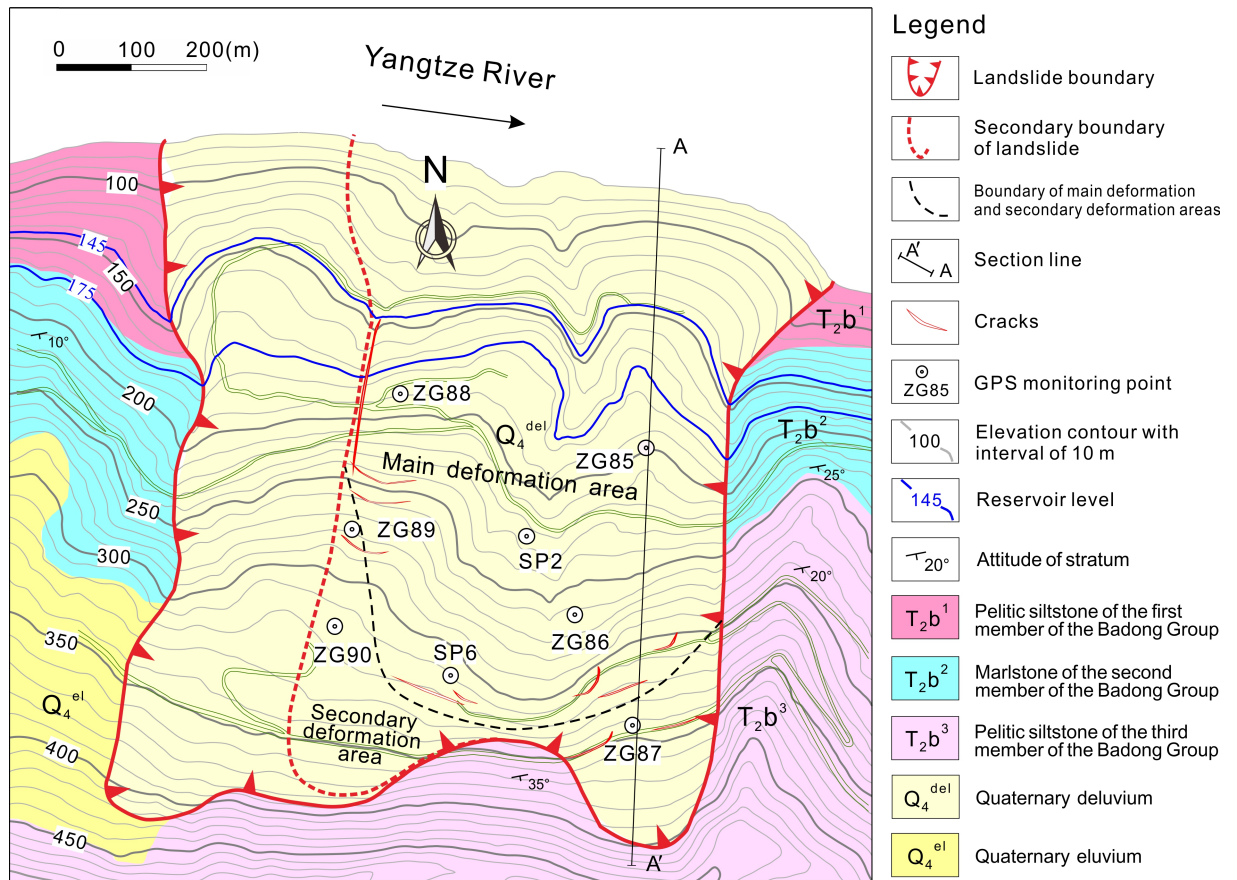
217 the deformation. This study provides a detailed geomechanical model that includes seepage and
218 buoyancy effects to clarify the deformation mechanism of this landslide which is calibrated by
219 long-term monitoring data.

220 **3.1 Geological setting**

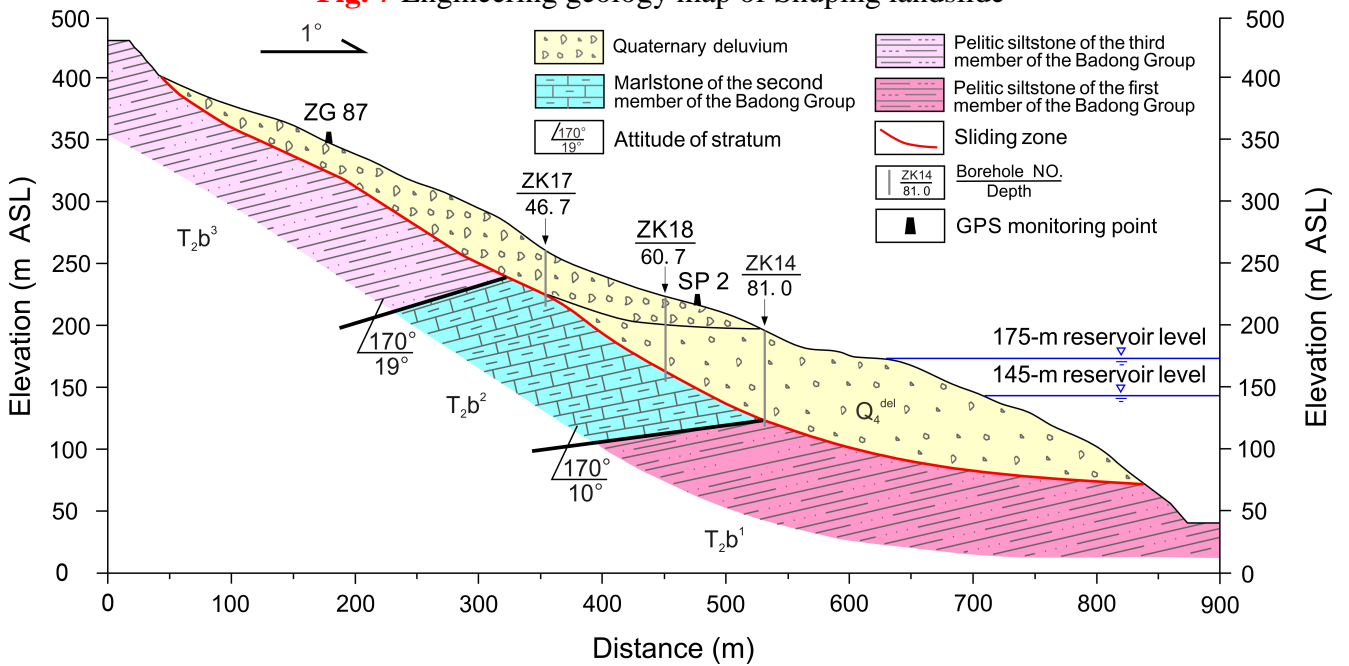
221 The Shuping landslide is a chair-shaped slope that dips 20° to 30° to the north, toward the
222 Yangtze River. The landslide is bounded on the east and west by two topographic gutters. The
223 altitude of its crown is 400 m above sea level (ASL), while its toe is about 70 m ASL, which is now
224 submerged by the reservoir, level of which varies annually between 145 and 175 m ASL (Fig. 7).
225 Borehole and inclinometer data (Lu et al. 2014) indicate that there are two major slide surface within
226 the west part of the slope and the upper rupture zone divides the slide mass into two parts (see Fig. 7).
227 The whole slide mass has a thickness of 30-70 m, a N-S length of about 800 m and W-E width of
228 approximately 700 m, constituting a total volume of ~27.5 million m³, of which 15.8 million m³
229 represents the main slide mass.

230 Shuping landslide is situated on an anti-dip bedrock of marlstone and pelitic siltstone of the
231 Triassic Badong Group (T₂b) (Fig. 8). The upper part of the slide mass is mainly composed of yellow
232 and brown silty clay with blocks and gravels, while the lower part of the slide mass mainly consists
233 of dense clay and silty clay with gravels, with a thickness of about 50 m on average. The deep
234 rupture zone is a 0.6~1.7 m layer that extends along the surface of bedrock, and consists of
235 yellowish-brown to steel gray silty clay. The upper rupture zone in the west part has similar
236 composition and has an average thickness of 1.0-1.2 m. The dip angle of the slide surface decreases
237 gradually from the rear to the front (Fig. 8), so the driving-resisting model is appropriate for Shuping
238 landslide. Before reservoir impoundment, boreholes ZK17 and ZK18 were dry but borehole ZK14

239 contained groundwater near the rupture zone.



240 **Fig. 7** Engineering geology map of Shuping landslide



241 **Fig. 8** Geological profiles along section A-A' as shown in Fig. 7

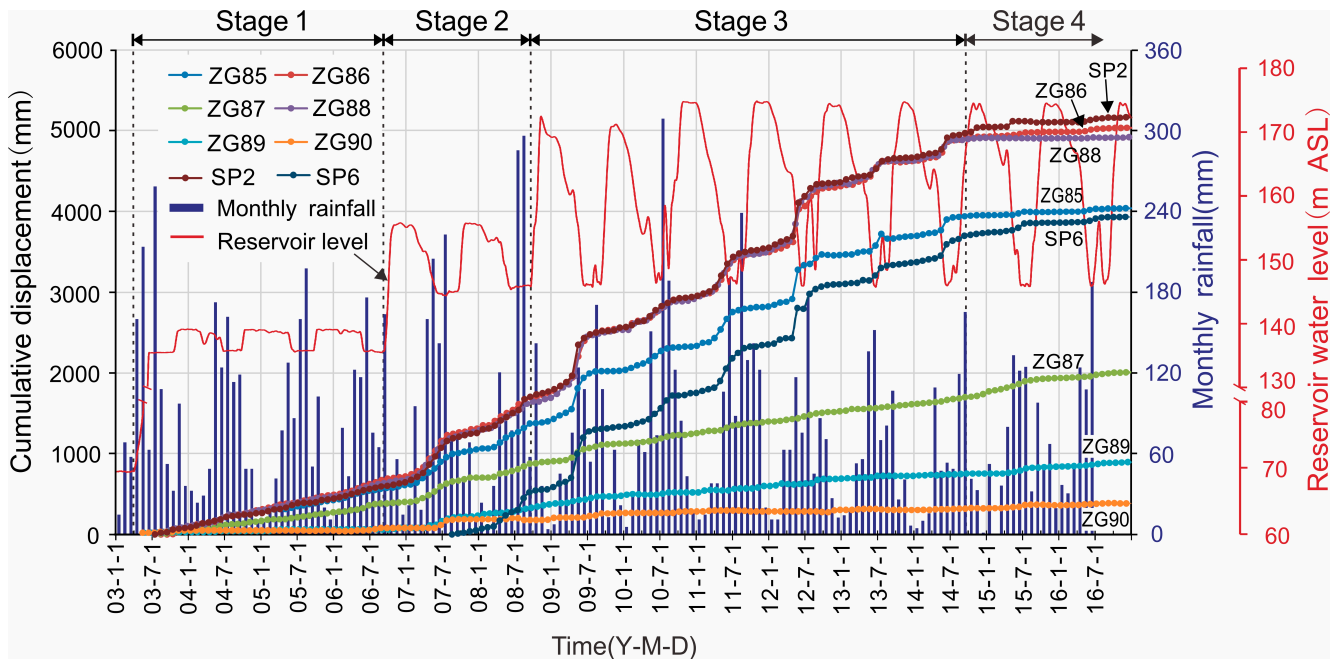
244 **3.2 Monitoring instrumentation**

245 The displacement monitoring system of Shuping landslide consists of 11 global positioning
246 system (GPS) survey points, three of which are datum marks that were installed on stable ground
247 outside the landslide area with the remainder being on the main slide mass (Fig. 7). Seven of the GPS
248 monitoring points (SP2, ZG85, ZG86, ZG87, ZG88, ZG89 and ZG90) were set in June 2003 and
249 GPS monitoring points SP6 was set in August 2007. All the GPS monitoring points were surveyed
250 every half month, and the system was upgraded to automatic, real-time monitoring in June 2012. The
251 daily rainfall records are obtained from the Meteorological Station near the Shuping landslide. Daily
252 reservoir level is measured by China Three Gorges Corporation (source:
253 <http://www.ctg.com.cn/inc/sqsk.php>).

254 **3.3 Engineering activity**

255 The evolution of Shuping landslide is related to four stages of human activity (Fig. 9). The first
256 stage was the 139 m ASL trial reservoir impoundment (from April 2003 to September 2006). The
257 reservoir water level was lifted from 69 to 135 m ASL and then changed between 135 and 139 m
258 ASL. The second stage was 156 m ASL trial reservoir impoundment (from September 2006 to
259 September 2008). The reservoir water level was raised from 139 to 156 m ASL, and then varied
260 annually between 145 and 156 m ASL. The third stage was 175 m ASL trial reservoir impoundment.
261 This stage began when the reservoir water level was raised to 175 m ASL, and thereafter managed to
262 annually varied between 145 and 175 m ASL (Tang et al., 2019). During the fourth stage, an
263 engineering project for controlling the deformation of Shuping landslide was conducted in

264 September 2014 and completed in June 2015 (see Section 6 for detailed description).



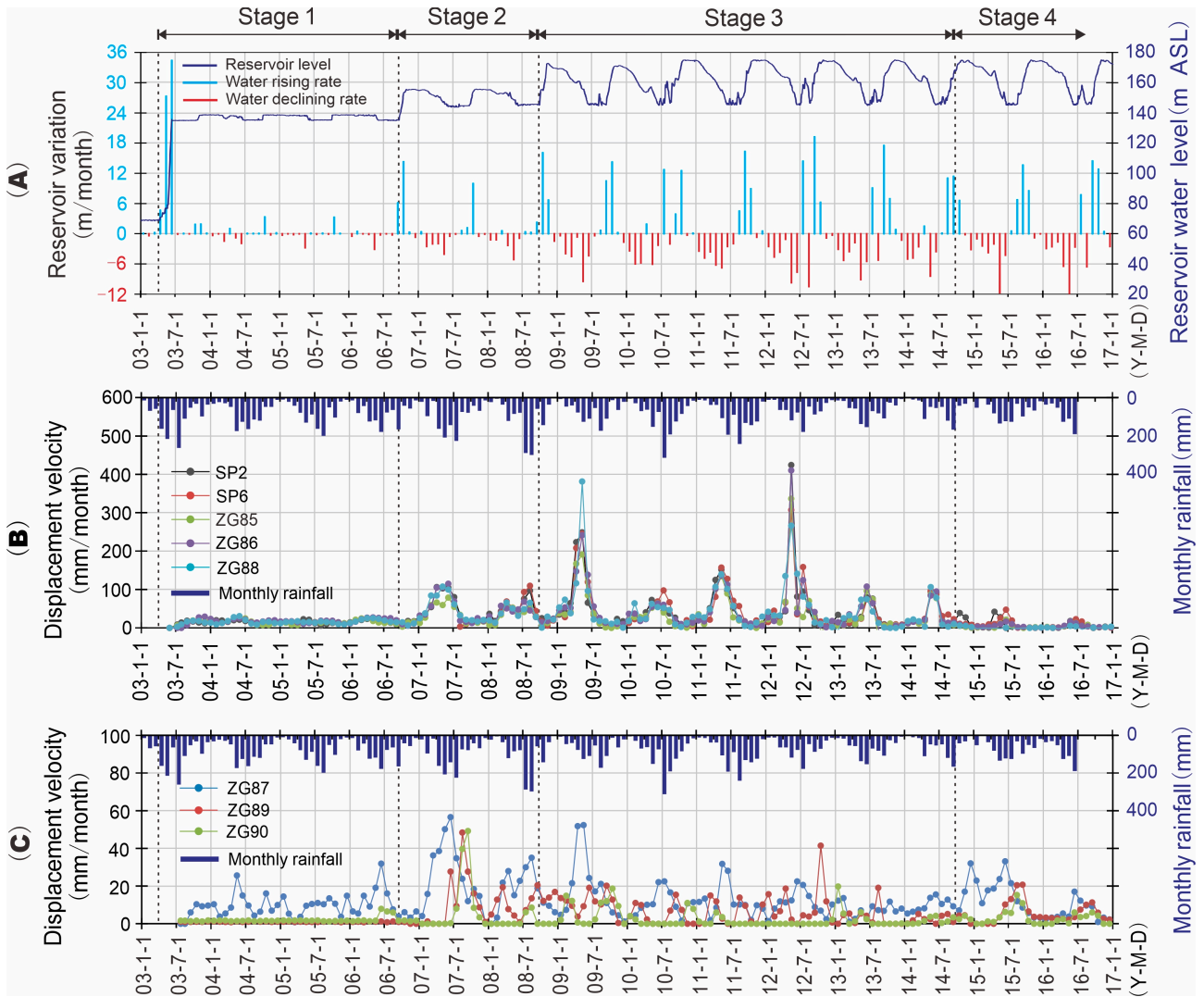
265
266 **Fig. 9** Monitoring data for Shuping landslide from 2003 to 2016.

267 **4 Field observational results**

268 **4.1 Overall deformation feature**

269 According to the deformation features revealed by the GPS monitoring system (Fig. 9, Fig. 10)
270 and field investigations, the main slide mass can be divided into a main deformation area and a
271 secondary deformation area (Fig. 7). The main deformation area underlies most of the area and has a
272 cumulative displacement up to 4-5 m, as measured at sites ZG85, ZG86, ZG88, SP2 and SP6. During
273 the 13-year monitoring period point SP2 underwent the largest cumulative displacement (5.168 m),
274 followed by ZG86 and ZG88 which recorded 5.039 m and 4.919 m, respectively. Deformations were
275 essentially synchronous at the monitoring sites as indicated by the similar shape of their cumulative
276 displacement curves, which typically show steady rises in the first impoundment stage, step-like
277 trends in the second and third impoundment stages, and flat trends after the engineering treatment.

278 Deformations were smaller and steadier in the secondary deformation area, as indicated by gentle
 279 cumulative displacement curves at ZG89, ZG90, and ZG87, which recorded cumulative
 280 displacements of 0.5-2 m during 2003 to 2016.



281
 282 **Fig. 10** Time series of reservoir level, rainfall and landslide displacement from 2003 to 2016. (A)
 283 Reservoir water levels and variation rates (positive for level rise, negative for level drop); (B)
 284 Displacement velocity of the GPS points in the main deformation area and monthly rainfall; (C)
 285 Displacement velocity of the GPS points in secondary deformation area and monthly rainfall.

286 **4.2 Deformation feature in different stages**

287 After the reservoir level first rose to 135 m ASL in June 2003, the main deformation area

288 deformed at an average velocity of 15.6 mm/month until September 2006, with each site recording
289 rather steady displacement curves whose tiny or nonexistent steps correspond to the small annual
290 variations in reservoir level. In contrast, no obvious deformation occurred during Stage 1 at ZG89
291 and ZG90 in the secondary deformation area.

292 During the earliest two months of Stage 2 (September, October 2006), when the reservoir level
293 first rose to 156 m ASL, displacement velocities of the main deformation area decreased to 13.4 and
294 9.7 mm/month respectively, indicating that slide mass stability had improved. For the next two
295 months (November, December) the velocity increased to 11.5 and 14.3 mm/month, as the reservoir
296 level was steady at 156 m ASL. During the subsequent drawdown period when the reservoir level
297 dropped to 145 m ASL in 2007, the displacement velocity increased to a maximum of about 100
298 mm/month (Fig. 10), resulting in an average “jump” of 458 mm in the cumulative displacement
299 curve, which then became flat while the reservoir remained at 145 m (Fig. 9).

300 During the beginning of Stage 3 when the reservoir first rose to nearly 175m in October 2008,
301 the displacement velocity of the main deformation area decreased to 12.7 mm/month, compared to
302 65, 74, 32 mm/month in the previous three months. Shortly after the reservoir rose to its highest level,
303 the level underwent a gradual decline and the displacement velocity increased steadily. The
304 maximum displacement velocity reached 378.6 mm/month at ZG88 in May 2009 when the water
305 level declined rapidly, a rate almost four times higher than when the reservoir dropped from 156 to
306 145 m ASL in 2007. Then the displacement velocity decreased to a relatively low value when the
307 water level was steady at 145 m ASL (Fig. 10B).

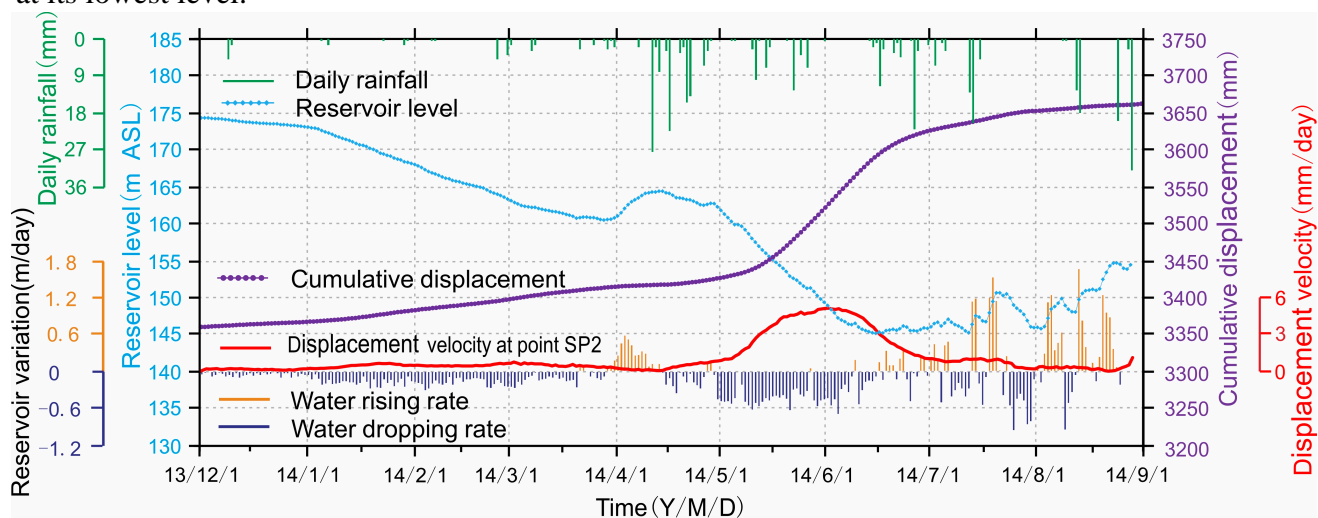
308 In the subsequent 6 years of Stage 3 the reservoir level underwent a series of similar annual
309 variations, and the slide mass responded with a series of deformation “jumps”. During these cycles,
310 the displacement velocity decreased as the reservoir rose, maintained low values when the reservoir
311 remained high, began to increase as drawdown began, and attained the values up to 165 mm/month
312 when drawdown was rapid. The corresponding cumulative displacement curves featured obvious
313 “jumps” during drawdown periods, then became relatively flat as the reservoir was maintained at the
314 low level of 145 m ASL. Clearly, these results show that displacement velocity is high during
315 reservoir drawdown and low during reservoir rise.

316 After the engineering treatment was completed in June 2015, the “jumps” in the cumulative
317 displacement curves disappeared and the curves became very flat (Fig. 9). The deformation was
318 reduced to a low level of 4.1 mm/month in the main deformation area, demonstrating effective
319 treatment.

320 **4.3 Effect of water-level fluctuation and rainfall on the deformation of Shuping landslide**

321 The largest “jump” in the cumulative displacement curves averaged 479 mm and occurred in
322 May to June, 2012, while the second was the jump of 458 mm in May to June, 2009. These periods
323 corresponded with the two highest drawdown rates of 9.67 and 9.38 m/month, respectively (Fig.
324 10A). During these two years, rainfall amounts were relatively low with monthly maxima of 180
325 mm/month in 2009 and 190 mm/month in 2012 (Fig. 10). These data clearly demonstrate that the
326 deformation of Shuping landslide is primarily driven by reservoir level variations and not by rainfall.
327 This relationship is also confirmed by the low displacement velocities and flat cumulative

328 displacement curves during the July and August peak of the rainy season, when the reservoir is held
 329 at its lowest level.



330
 331 **Fig. 11** Monitoring data of GPS point SP2 on the middle part of slide mass, from December 2013 to
 332 September 2014.

333 **Figure 11** clarifies the influence of reservoir level and rainfall on landslide deformation. In
 334 December 2013, the reservoir level dropped at an average rate of 0.041 m/day, and the corresponding
 335 displacement velocity was 0.22 mm/day. In the subsequent three months, the drawdown rate of the
 336 reservoir level increased to 0.147 m/day, and the displacement velocity rose to 0.54 mm/day. During
 337 March 2014, the displacement velocity decreased as the water level increased, even though intense
 338 rainfalls were recorded during this period (up to 27.5 mm/day). In the following rapid drawdown
 339 period (0.419 m/day) from May to June, the displacement velocity increased to about 5 mm/day.
 340 Subsequently, the displacement velocity decreased to less than 1.2 mm/day as the water level
 341 remained low, although rainfall was abundant. These details confirm that the displacement velocity
 342 of the Shuping landslide is positively related to the drop rate of the reservoir, with rainfall having
 343 little effect.

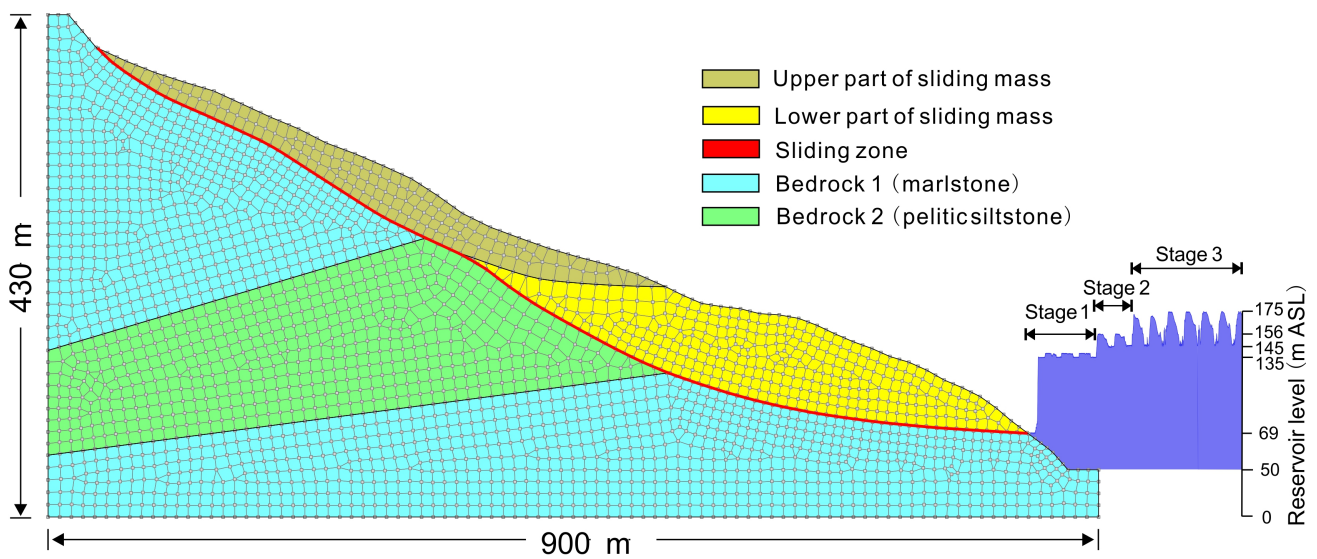
344 Unlike the flat displacement curves and low displacement velocity in other years when the
345 reservoir level was steady at the lowest annual level in July and August, displacement velocities were
346 large in 2008 and 2010 (65.0 and 73.8 mm/month in July and August 2008; 58.4 mm/month in July
347 2010, about half of the average highest monthly displacement velocity, 165 mm/month, during rapid
348 draw down period). Very heavy rainfall was recorded during those periods, up to 300 mm/month.
349 However, August 2011 had the next heaviest rainfall of 250 mm/month, yet the cumulative
350 displacement curve remained flat and the displacement velocity was low (22.2 mm/month). These
351 data illustrate that heavy rainfall can decrease landslide stability and accelerate deformation, but
352 nevertheless is a secondary factor. The difference in the displacement velocity between the months
353 with the highest (2008, 2010) and the second highest (2011) levels of rainfall suggests that a
354 threshold exists, with rainfall exceeding this value having a significant effect but with less having
355 little significance. This threshold appears to be about 250-300 mm/month.

356 **5 Numerical simulation**

357 In this section, groundwater flow in the Shuping slope under the variation of the reservoir level
358 is simulated to assist the driving-resisting model to explain the deformation process of Shuping
359 landslide. Seepage simulation is performed by the SEEP/W module of GEOSTUDIO software (see
360 <http://www.geoslope.com>). The deformation state of the landslide is usually regarded as the
361 performance of the landslide stability state (Wang et al., 2014; Huang et al., 2017). Thus, the *Fos*
362 (Safety of factor) of the Shuping landslide is calculated with the simulated groundwater level, to
363 evaluate the stability of the Shuping landslide under various impoundment scenarios. In this study,

364 the Fos of the Shuping landslide is calculated by Morgenstern-Price method (Zhu et al., 2005) using
 365 the SLOPE/W module of GEOSTUDIO software. The external impoundment load affect is
 366 considered by this software. Different evaluation method for landslide stability will lead to different
 367 value of Fos ; thus we only employ the calculated values of Fos to investigate the variation trend of
 368 the landslide stability.

369 **Figure 12** shows the numerical simulation model of the Shuping landslide, whose framework is
 370 based on the geological profile map in **Fig. 8**. The slope was divided into six regions composed of
 371 five materials with different properties (Table 1). Zero flux boundary conditions were assigned along
 372 the bottom horizontal and the right vertical boundaries. **A constant water head was applied at the left**
 373 **vertical boundary according to the water table in the borehole**. The optimum water head at the left
 374 boundary is 230 m ASL. The hydrograph of TGR from January 1, 2003 to September 10, 2014 (**Fig.**
 375 **13(A)**) and generalized hydrograph of the trial impoundment at 175 m ASL (**Fig. 13(B)**) were used to
 376 define the right boundary adjacent to the reservoir. Initial conditions were defined using the water
 377 tables revealed by boreholes.



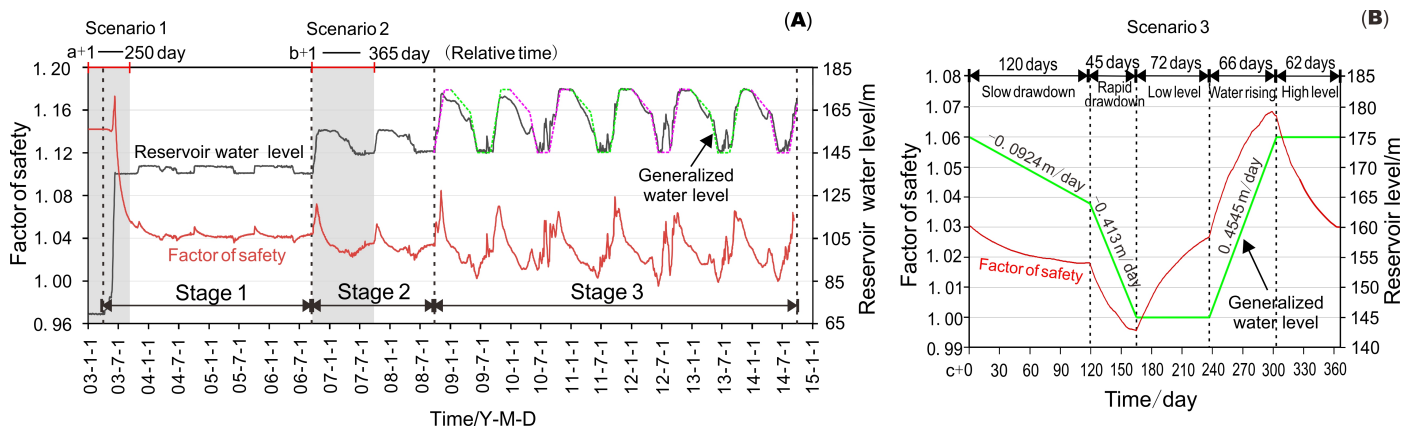
378
 379 **Fig. 12** Numerical simulation model of seepage for Shuping landslide.

Table 1 Hydrologic and mechanical properties of Shuping landslide

Location	Material	Saturated conductivity k_s (m/day)	Residual volumetric water content θ_r	Saturated volumetric water content θ_s	Fitting parameter in the van Genuchten's model α	Fitting parameter in the van Genuchten's model n	Unit weight γ (kN/m ³)	cohesion c' (kPa)	friction angle ϕ' (°)
Upper part of slide mass	Silty clay with blocks and gravels	4.95 ^a	0.129	0.39	0.141	1.869	20.3 ^a	/	/
Lower part of slide mass	Silty clay with gravels	3.90 ^a	0.129	0.39	0.141	1.869	20.3 ^a	/	/
Rupture zone	Silty clay	2.98×10^{-2} ^b	0.08	0.30	0.035	1.758	/	25.7 ^a	20.4 ^a
Bedrock 1	Marlstone	1.47×10^{-4} ^b	0.05	0.20	0.0173	1.606	/	/	/
Bedrock 2	Pelitic siltstone	8.99×10^{-5} ^b	0.05	0.20	0.0173	1.606	/	/	/

381 ^a Provided by Hubei Province Geological Environment Terminus (2003)

382 ^b Values of similar material from literature (Hu et al., 2015)



383

384 **Fig. 13** (A) Time series of reservoir level and corresponding calculated *Fos* of Shuping landslide

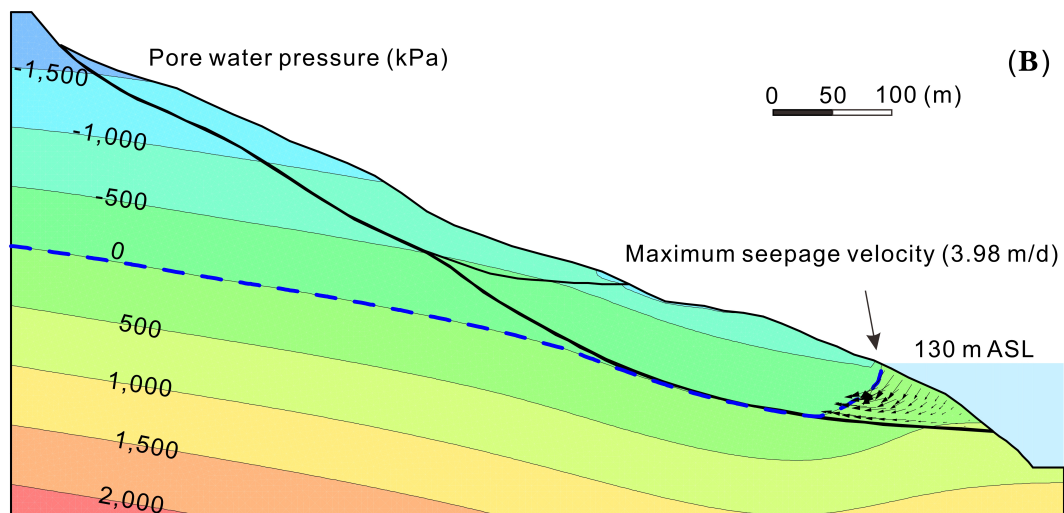
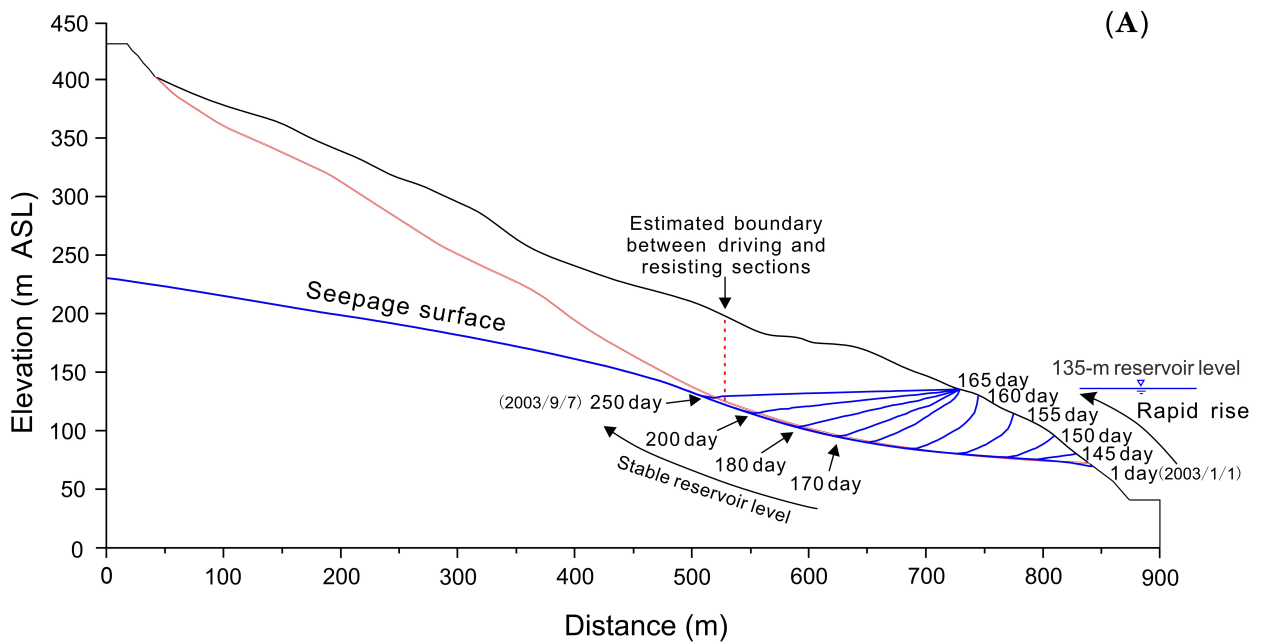
385 from January 1, 2003 to September 10, 2014. (B) Generalized annual variation curve of the reservoir

386 level obtained by fitting the real water level from 2008 to 2014 (Stage 3) and the corresponding time

387 series of the calculated *Fos* of Shuping landslide.

388 **5.1 Scenario 1: first trial impoundment at 139 m ASL**

389 From April 10 to June 11, 2003 (a+100~162 day), the reservoir level rose rapidly from 69 to 135
390 m ASL. Fig. 14 shows that, during this period, groundwater storage increased in the toe of the slide
391 mass and within the lower part of the resisting section, increasing buoyancy forces that destabilized
392 the slope. In contrast, the inwardly-directed flow created a seepage force directed towards the slope
393 (Fig. 14(B)), increasing stability. Owing to the high hydraulic gradient, the stabilizing effect of the
394 seepage force on the slope prevails over the destabilization due to increased buoyancy, so slope
395 stability was improved during this phase, as indicated by the increase in Fos up to 1.17 (Fig. 13).



396
 397 **Fig. 14** (A) Simulated groundwater tables during the period of rapid reservoir rise from January 1,
 398 2003 to September 7, 2003; (B) simulated pressure contours and flow vector on June 19, 2003
 399 (a+170 day) during first impoundment period.

400 In the following period (a+163 day~), the reservoir level was maintained around 135 m ASL.
 401 The water table progressively rose until it approximated the reservoir level. During this period, the
 402 slope of the water table front decreased gradually (**Fig. 14(A)**), leading to the decrease of the seepage
 403 force in the slope. At the same time, the buoyancy uplift effect increased steadily in the resisting

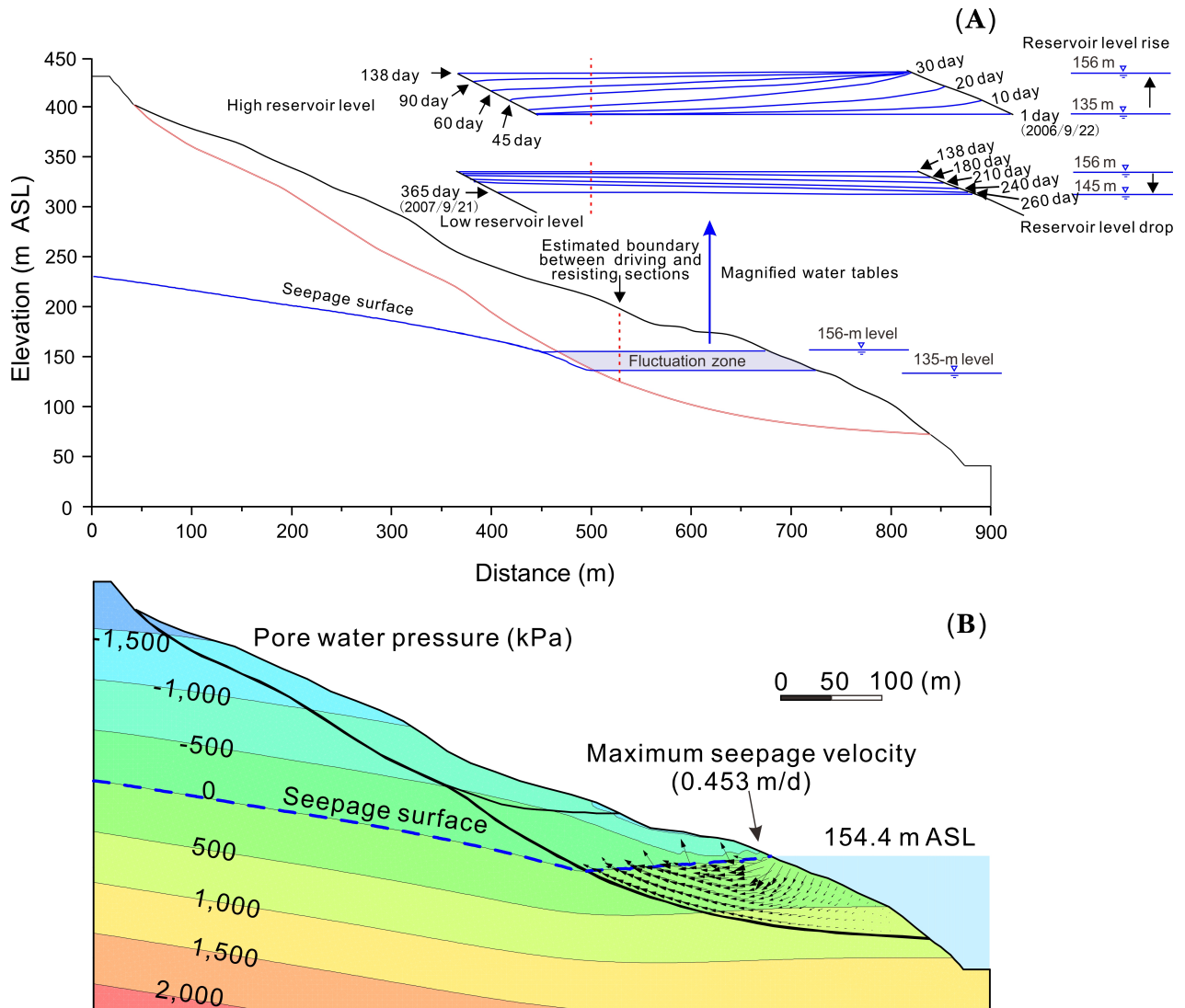
404 section as the groundwater table rose. The combination of a decreased seepage force and the
405 increased buoyancy led to a decrease in slope stability during this phase, so the Fos dropped below
406 its initial value of 1.142. Afterwards, the slope stability continued to decrease until the new but
407 temporary state of equilibrium was reached. The safety factor was around 1.045 as the reservoir level
408 was maintained around 135 m ASL.

409 The delay between the reservoir impoundment and the decrease in stability is consistent with the
410 creation of obvious cracks after the reservoir rose to 135 m ASL (Wang et al., 2007). The famous
411 Qianjiangping landslide (Fig. 2), which is located near the Shuping landslide and has similar
412 geological setting, occurred one month (13 July 2003) after the reservoir first rose to 135 m ASL
413 (Xiao et al., 2007).

414 **5.2 Scenario 2: first trial impoundment at 156 m ASL**

415 During the periods when the water level rose from 135 m ASL to 156 m ASL (b+1~30 day) (Fig.
416 15), and stayed stable at 156 m ASL (b+30~138 day), the effects of ground water level change on the
417 stability of Shuping landslide were similar to the effects in scenario 1. When the reservoir level
418 dropped from 156 to 145 m ASL during the drawdown period of February to June (b+138~260 day),
419 groundwater flow towards the reservoir (Fig. 15(B)), thus creating an outward, destabilizing seepage
420 force on the slope. The computed factor of safety decreased gradually from 1.070 to 1.025, in
421 agreement with the observed increase in displacement velocity during this period. As the reservoir
422 level was then maintained at 145 m ASL (b+260~365 day), the transient seepage gradually
423 transitioned to steady-state seepage, accompanied by a progressively decline of the water table in the

424 inside part of the fluctuation zone, a weakening of the destabilizing effect of the seepage force, and a
 425 result of increase in slope stability ($Fos=1.035$).



426
 427 **Fig. 15** (A) Simulated groundwater tables as the variation of reservoir water level from 22 September
 428 2006 to 21 September 2007; (B) simulated pressure contours and flow vector on July 11, 2007 (day
 429 b+260) during drawdown period

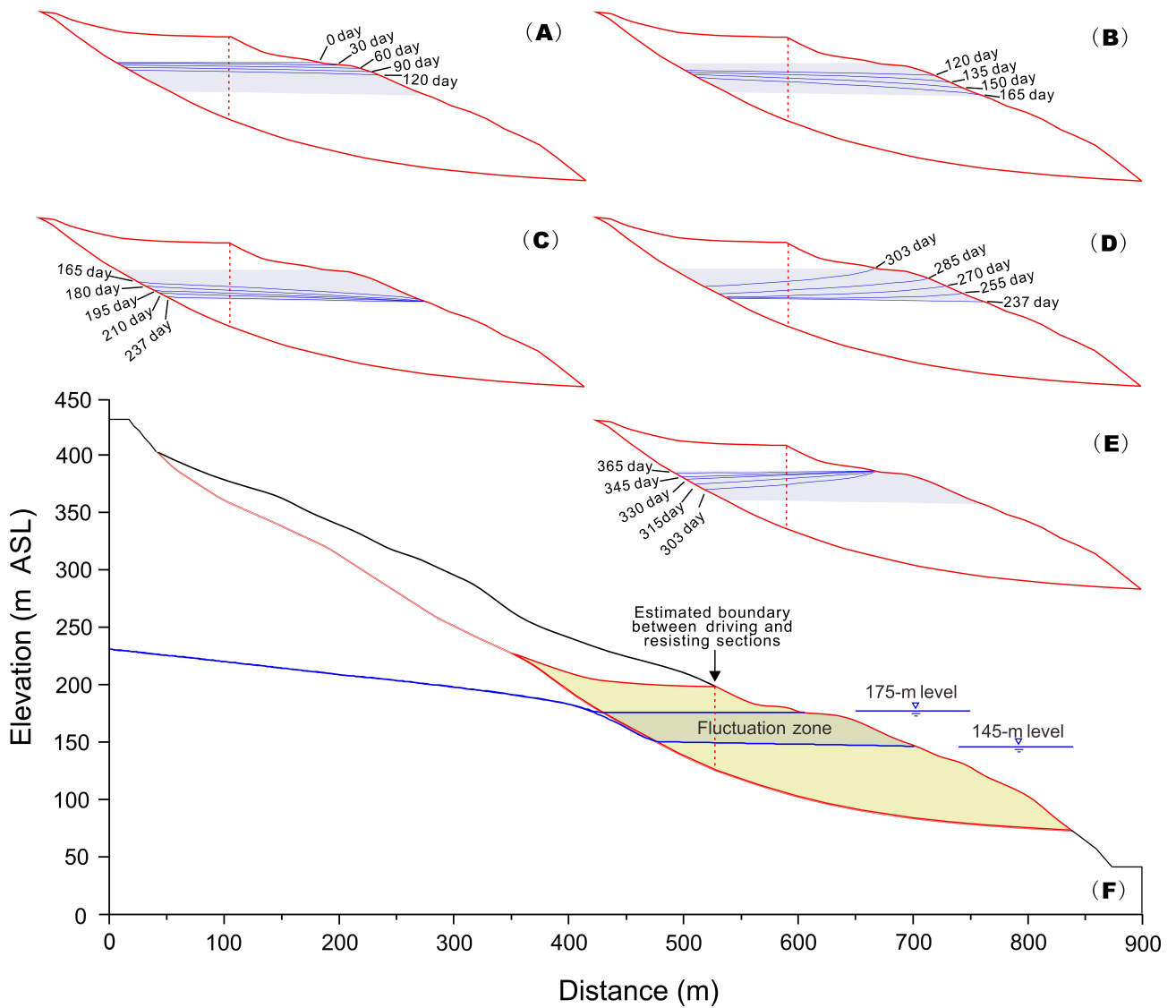
430 **5.3 Scenario 3: trial impoundment at 175 m ASL**

431 During 2008 to 2014 the reservoir level periodically fluctuated between 145 and 175 m ASL
 432 (Stage 3), in accordance with a generalized annual water level variation curve that consists of five

433 phases (Fig. 13(B)).

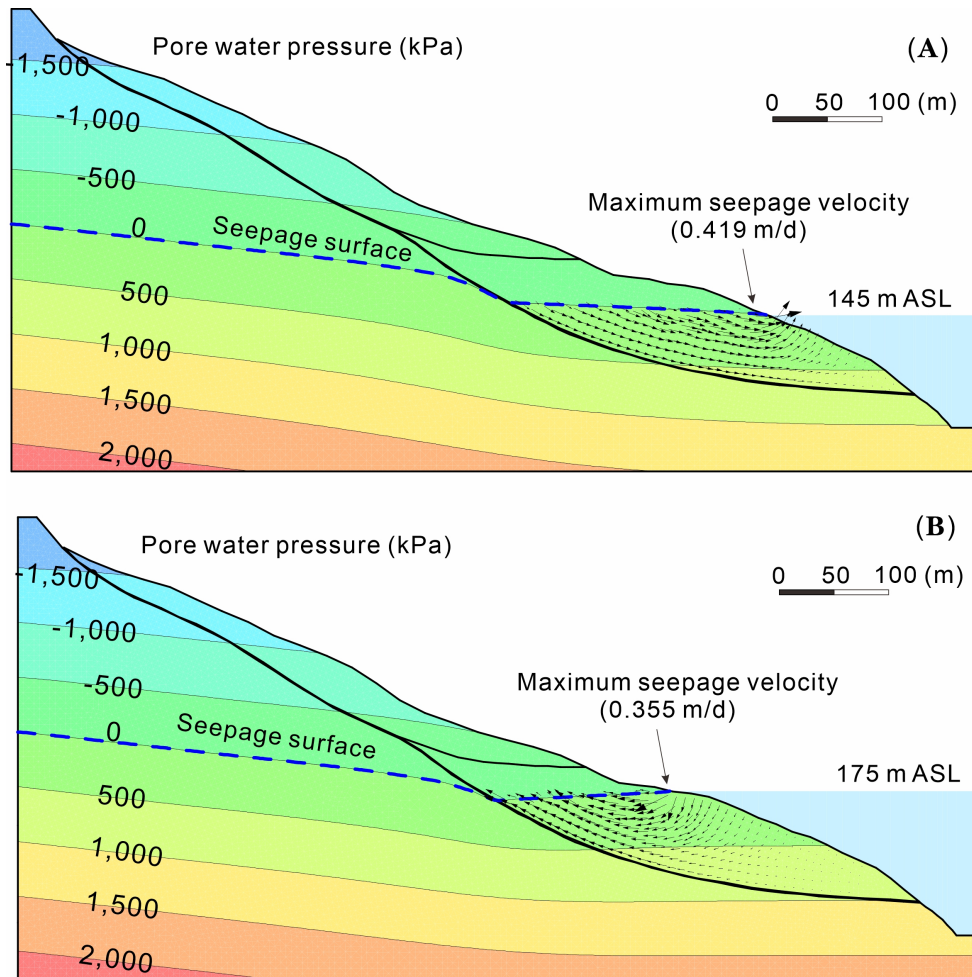
434 During the slow drawdown period, the groundwater storage in the driving section is reduced by
435 an amount that approximately matches the reduction in the resisting section (Fig. 16(A)), so the
436 effect of buoyancy forces on slope stability is small. Moreover, because drawdown is slow,
437 groundwater gradients are also low, limiting the magnitude of destabilizing seepage forces. Thus, the
438 safety factor of the slope decreases from 1.031 to 1.018 with only a modest amount (Fig. 13(B)).

439 During the rapid drawdown phase, groundwater gradients are steeper and produce large,
440 destabilizing seepage forces on the slope (Fig. 17(A)). The sharp decline of slope stability (Fig.
441 16(B)) is consistent with the observed high displacement velocity during this phase. The slope
442 stability becomes least ($Fos=0.995$) as the reservoir declines to its lowest level of 145 m ASL, when
443 a maximum difference of 14 m is computed for groundwater levels in the slide mass (Fig. 16(B)).
444 Although the decreased buoyancy of the resisting section makes an offsetting contribution to slope
445 stability, its magnitude is small compared to that of destabilizing seepage forces.



446

447 **Fig. 16** Simulated groundwater tables over the period of generalized annual variation of reservoir
 448 water level in Stage 3. Gray shaded zone depicts the 145 to 175 m elevation interval. (A) slow
 449 drawdown phase; (B) rapid drawdown phase; (C) low level phase; (D) water level rising phase; (E)
 450 high water level phase



451

452 **Fig. 17** (A) Simulated pressure contours and flow vector at the end of rapid drawdown period (day
 453 165 in Fig. 16); (B) Simulated pressure contours and flow vector at the begin of high level period
 454 (day 303 in Fig. 16)

455

456

457

458

459

460

461

In the following three phases, representing the low water, rising and high water phases, the characteristics of the slope vary in a manner similar to those modeled in scenario 2. The stability of the landslide (see Fig. 13(B)) recovers gradually from 0.995 to 1.027 in the low water level phase, due to the dissipation of destabilizing seepage forces (Fig. 16(C)). Slope stability then increases rapidly as the reservoir level rises rapidly, when the seepage force reverses to become directed into the slope (Fig. 16(D), Fig. 17(B)). The slope obtains the highest stability with Fos value of 1.067 when the water level rises to the highest level 175 m ASL. Slope stability then decreases gradually as

462 that seepage force declines (Fig. 16(E)). All these results agree with the observed variations in
463 displacement velocity of the Shuping landslide (Sec. 4.2).

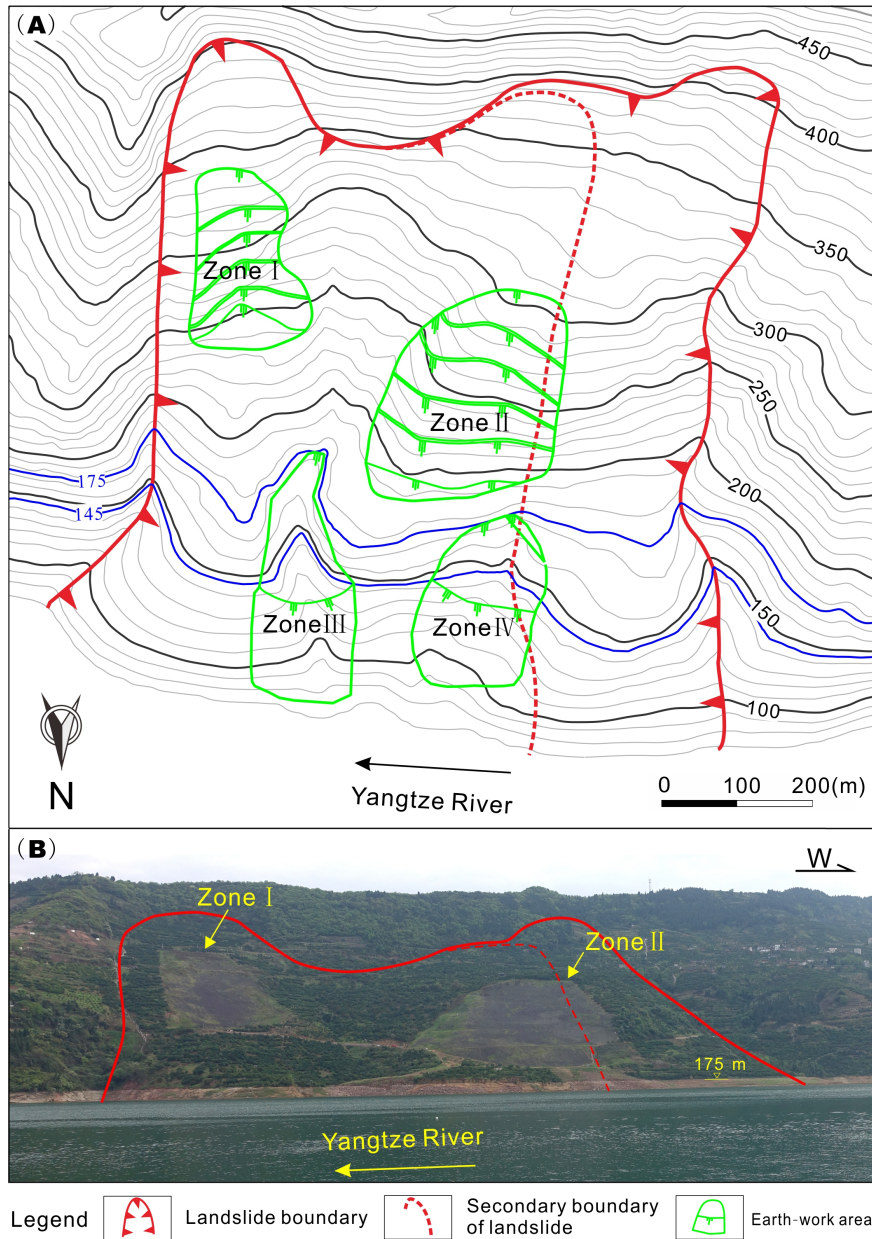
464 In summary, during periods of reservoir drawdown and rise, the seepage force plays a dominant
465 role in the stability of Shuping landslide, but being negative in drawdown period and positive in the
466 rising period. In contrast, buoyancy effects become increasingly important during periods of steady
467 reservoir levels, as seepage forces steadily decrease.

468 **6 Discussion**

469 The deformation of the Shuping landslide is a function of reservoir levels but probably also
470 depends on the hydraulic character of its constituent material. The lower part of the slide mass that is
471 subject to reservoir level fluctuation is mainly composed of dense silty soil with very low hydraulic
472 conductivity. During periods of rapid change in reservoir level, large differences in groundwater head
473 can be formed in such material, generating large seepage pressures that can either destabilize or
474 stabilize the mass, depending on whether the reservoir is rising or falling. On the other hand, low
475 permeability materials impede rainfall infiltration, rendering the landslide little influenced by rainfall.
476 Consequently, variations of the reservoir level and their attendant seepage forces dominate the
477 deformation of Shuping landslide.

478 Based on this observation and on the results of the driving-resisting model, two approaches are
479 recommended to control the deformation of huge reservoir landslides where the reinforcement
480 structures are difficult to construct. One method to improve stability is to transfer earth mass from
481 the driving section to the resisting section of the slide mass. The other is to use drains or pumps to
482 lower the water levels inside the slope, in order to reduce differences in groundwater head during

483 periods of reservoir drawdown. The first approach has in fact been adopted to enhance the stability of
484 Shuping landslide, which was conducted in September 2014 and completed in June 2015. Fig. 18(A)
485 presents the layout of the engineering treatment and Fig. 18(B) is the subsequent photo of Shuping
486 landslide. Zones I and II are the areas of load reduction, located in the driving section of the
487 slide mass. The earth mass of Zone I ($\sim 1.8 \times 10^5 \text{ m}^3$) and Zone II ($\sim 4.0 \times 10^5 \text{ m}^3$) were transferred
488 to Zones III and IV respectively, which are located in the resisting section that is mostly below
489 reservoir level in the photo (Fig. 18(B)). Monitoring data show that the displacement velocity was
490 significantly reduced to low values (about 4.1 mm/month in the main deformation area),
491 demonstrating the effectiveness of the engineering treatment. These approaches are more economical
492 and require a shorter construction period than many commonly-used remediation methods such as
493 the construction of stabilizing piles. Most importantly, these treatments are feasible for many other
494 large reservoir landslides.



495

496 **Fig. 18** Topography of Shuping landslide before (A) and after (B) engineering treatment, which

497 involved the transfer of earth from Zones I and II to Zones III and IV.

498 The determination of the position of the boundary between driving and resisting sections is very

499 complicated as it is related many factors. As the reservoir level varies, the stress of the landslide

500 changes, which can affect the position of the boundary, and the position is dynamic. In this study, we

501 proposed a static criterion to estimate the boundary position, that is, the boundary between the

502 resisting and driving sections can be approximated as the position where the slope angle of the slide

503 surface equals the internal friction angle ϕ of the slide surface (section 2.2). This criterion was
504 effectively adopted to interpret the deformation process of the Shuping landslide.

505 The frictional property of the sliding surface is an important factor affecting the landslide
506 stability and the position of the boundary of the driving and resisting sections. The slip zone soil
507 commonly displays a strain softening behaviour, indicating the soil strength generally evolves into
508 peak strength and the residual strength after large deformations (Skempton, 1985). Many researches
509 (Liu, 2009; Tang et al., 2015;) also aware that the frictional property of the slip surface varies in
510 space. For example, the retrogressive landslides, such as Zhujiadian landslide in the TGRA (Hu et al.,
511 2015), the front part has larger displacement than that in the rear part, leading to the resisting shear
512 strength is less than that in the rear part (Tan et al., 2016), and the resisting section is unlikely formed
513 in these landslides. While, in the progressive landslides, such as Jiweishan landslide (Tang et al.,
514 2015), the front part experiences less deformation than that in the rear part, and the front part has
515 relative high shear strength, forming the resisting section. In some landslides, such as the Huangtupo
516 landslide, Baishuihe landslide and Ganjuyuan landslide (see Fig. 1), the sliding surfaces are irregular,
517 which definitely increase the overall friction of the slip surface and increase the insisting section. In
518 the situation that the sliding surface is irregular and the shear strength of the sliding surface varies
519 obviously in space, a more rigorous method is required to determinate the boundary position.

520 **7 Conclusions**

521 A driving-resisting model is presented to elucidate the deformation mechanism of reservoir
522 landslides, as exemplified by Shuping landslide. The displacement velocity of Shuping landslide is

523 closely related to the variations in the level of the Three Gorges reservoir. Rainfall effects are limited
524 in comparison, perhaps due to the low hydraulic conductivity of the slide material. Rapid reservoir
525 drawdown produces large, destabilizing seepage forces in the slope of the slide mass, as evidenced
526 by large increases of its displacement velocity. In contrast, rising reservoir levels reverse the
527 direction of the seepage force, improving slope stability and decreasing the displacement velocity.
528 The buoyancy effect on the resisting section decreased the slope stability when the reservoir first rose
529 to 135 m ASL, but this effect has diminished as the reservoir has attained higher levels that buoy
530 both the driving and resisting sections.

531 Monitoring data, the driving-resisting model, and a successful engineering treatment suggest two
532 means to increase the stability of landslides in the TGR area. Recommended approaches are: 1)
533 transferring earth mass from the driving section to the resisting section; and 2) lowering the ground
534 water levels inside the slope by drains or by pumping during periods of reservoir drawdown. The
535 first approach was successfully applied to the Shuping landslide and could be used to treat many
536 other huge landslides in the Three Gorges Reservoir area.

537 **Data availability**

538 The study relied on the observation data from Department of Land and Resources of Hubei
539 Province, China.

540 **Competing interests**

541 The authors declare that they have no conflict of interest.

542 **Acknowledgements**

543 This work was supported by the National Key R&D Program of China (No. 2017YFC1501305);
544 the Fundamental Research Funds for the Central Universities, China University of Geosciences
545 (Wuhan) (No. CUGCJ1701); and the National Natural Science Foundation of China (Nos. 41630643,
546 41827808, 41502290).

547

548 **9 References**

- 549 1. Baum, R.L., and Fleming, R.W.: Use of longitudinal strain in identifying driving and resisting
550 elements of landslides, *Geol. Soc. Am. Bull.* 103, 1121–1132, 1991
- 551 2. Casagli, N., Rinaldi, M., Gargini, A. and Curini, A.: Monitoring of pore water pressure and
552 stability of streambanks: results from an experimental site on the Sieve River, Italy, *Earth Surface
553 Processes and Landforms*, 24, 1095-1114, [https://doi.org/10.1002/\(SICI\)1096-9837\(199911\)24:
554 12<1095::AID-ESP37>3.0.CO;2-F](https://doi.org/10.1002/(SICI)1096-9837(199911)24:12<1095::AID-ESP37>3.0.CO;2-F), 1999.
- 555 3. Chang, S.B., Zhang, S.M. and Xiang B.: *Engineering geology manual*. China Architecture &
556 Building Press, Beijing, 2007 (in Chinese).
- 557 4. Cojean, R. and Cai, Y.J.: Analysis and modeling of slope stability in the Three-Gorges Dam
558 reservoir (China) -The case of Huangtupo landslide, *Journal of Mountain Science*, 8, 166-175,
559 <https://doi.org/10.1007/s11629-011-2100-0>, 2011.
- 560 5. Du, J., Yin, K., and Lacasse, S.: Displacement prediction in colluvial landslides, three Gorges
561 reservoir, China, *Landslides*, 10, 203-218, <https://doi.org/10.1007/s10346-012-0326-8>, 2013.
- 562 6. Dumperth, C., Rohn, J., Fler, A., and Xiang, W.: Local-scale assessment of the displacement
563 pattern of a densely populated landslide, utilizing finite element software and terrestrial radar
564 interferometry: a case study on Huangtupo landslide (PR China), *Environmental Earth Sciences*,
565 75, 880, <http://doi.10.1007/s12665-016-5475-y>, 2016.
- 566 7. Froude, M. J. and Petley, D. N.: Global fatal landslide occurrence from 2004 to 2016, *Natural
567 Hazards and Earth System Sciences*, 18, 2161-2181, <https://doi.org/10.5194/nhess-18-2161-2018>,
568 2018.

- 569 8. Guerriero, L., Coe, J.A., Revellino, P., Grelle, G., Pinto, F. and Guadagno, F.M.:
570 Influence of slip-surface geometry on earth-flow deformation, Montaguto earth flow, southern
571 Italy: *Geomorphology*, 219, 285-305, <http://dx.doi.org/10.1016/j.geomorph.2014.04.039>, 2014.
- 572 9. Handwerger, A.L., Roering, J., Schmidt, D.A., and Rempel, A.W.: Kinematics of earthflows in the
573 Northern California Coast Ranges using satellite interferometry, *Geomorphology*, 246, 321-333,
574 <https://doi.org/10.1016/j.geomorph.2015.06.003>, 2015.
- 575 10. Hu, X.L., Zhang, M., Sun, M.J., Huang, K.X. and Song, Y.J.: Deformation characteristics and
576 failure mode of the Zhujiadian landslide in the Three Gorges Reservoir, China, *Bulletin of*
577 *Engineering Geology and the Environment*, 74, 1-12, <https://doi.org/10.1007/s10064-013-0552-x>,
578 2015.
- 579 11. Hu, X.W., Tang, H.M. and Liu, Y.R.: Physical model studies on stability of Zhaoshuling landslide
580 in area of Three Gorges Reservoir, *Chinese Journal of Rock Mechanics and Engineering*, 24,
581 2089-2095, 2005 (in Chinese).
- 582 12. Huang, B.L., Yin, Y.P., Wang, S.C., Tan, J.M. and Liu, G.N.: Analysis of the Tangjiaxi
583 landslide-generated waves in the Zhexi Reservoir, China, by a granular flow coupling model,
584 *Natural Hazards and Earth System Sciences*, 17, 657-670,
585 <https://doi.10.5194/nhess-17-657-2017>, 2017.
- 586 13. Huang, D. and Gu, D.M.: Influence of filling-drawdown cycles of the Three Gorges reservoir on
587 deformation and failure behaviors of anacinal rock slopes in the Wu Gorge, *Geomorphology*,
588 295, 489-506, <https://doi.org/10.1016/j.geomorph.2017.07.028>, 2017.
- 589 14. Huang, F.M., Huang, J.S., Jiang, S.H. and Zhou, C.B.: Landslide displacement prediction based on

- 590 multivariate chaotic model and extreme learning machine, *Engineering Geology*, 218, 173-186,
591 <https://doi.org/10.1016/j.enggeo.2017.01.016>, 2017.
- 592 15. Hubei Province Geological Environment Terminus: Survey report of Shuping landslide in Three
593 Gorges Reservoir area, Zigui, Hubei Province, China, 2013 (in Chinese).
- 594 16. Hutchinson, J.N.: An influence line approach to the stabilization of slopes by cuts and fills,
595 *Canadian Geotechnical Journal*, 21, 363-370, <https://doi.org/10.1139/t84-036>, 1984.
- 596 17. Iverson, R.M.: Unsteady, nonuniform landslide motion: 2. Linearized theory and the kinematics of
597 transient response, *Journal of Geology*, 94, 349-364, <https://doi.org/10.1086/629034>, 1986.
- 598 18. Jia, G.W., Zhan, T.L., Chen, Y.M. and Fredlund, D.G.: Performance of a large-scale slope model
599 subjected to rising and lowering water levels, *Engineering Geology*, 106, 92-103,
600 <https://doi.org/10.1016/j.enggeo.2009.03.003>, 2009.
- 601 19. Junfeng Z., Xiangyue M. and Erqian Z.: Testing study on landslide of layered slope induced by
602 fluctuation of water level, *Chinese Journal of Rock Mechanics and Engineering*, 23, 2676-2680,
603 2004 (in Chinese).
- 604 20. Lambe, T.W. and Whitman, R.V.: *Soil mechanics SI version*, John Wiley & Sons, 2008.
- 605 21. Lane, P.A. and Griffiths, D.V.: Assessment of stability of slopes under drawdown conditions,
606 *Journal of geotechnical and geoenvironmental engineering*, 126, 443-450,
607 [https://doi.org/10.1061/\(ASCE\)1090-0241\(2000\)126:5\(443\)](https://doi.org/10.1061/(ASCE)1090-0241(2000)126:5(443)), 2000.
- 608 22. Li, D., Yin, K. and Leo, C.: Analysis of Baishuihe landslide influenced by the effects of reservoir
609 water and rainfall, *Environmental Earth Sciences*, 60, 677-687,
610 <https://doi.org/10.1007/s12665-009-0206-2>, 2010.

- 611 23. Liao, H.J., Sheng, Q., Gao, S.H. and Xu, Z.P.: Influence of drawdown of reservoir water level on
612 landslide stability, *Chinese Journal of Rock Mechanics and Engineering*, 24, 3454-3458, 2005 (in
613 Chinese).
- 614 24. Liu, C.N.: Progressive failure mechanism in one-dimensional stability analysis of shallow slope
615 failures, *Landslides*, 6, 129-37, <https://doi.org/10.1007/s10346-009-0153-8>, 2009.
- 616 25. Lu, S. Q., Yi, Q. L., Yi, W., Huang, H. F. and Zhang, G. D.: Analysis of deformation and failure
617 mechanism of Shuping landslide in Three Gorges reservoir area. *Rock and Soil Mechanics* 35(4),
618 1123-1130, 2014 (in Chinese).
- 619 26. Lu, T.: Study of Formation Mechanism and Later Trend Prediction of Fanjiaping Landslide and
620 Baishuihe Landslide, Dissertation, China Three Gorges University (in Chinese).
- 621 27. Ma, J. W., Tang, H. M., Hu, X. L., Bobet A., Zhang, M., Zhu, T. W., Song, Y. J. and Eldin M. A. E.:
622 Identification of causal factors for the Majiagou landslide using modern data mining methods,
623 *Landslides*, 14, 311-322, <https://doi.org/10.1007/s10346-016-0693-7>, 2017.,
- 624 28. McKean, J. and Roering, J.: Objective landslide detection and surface morphology mapping using
625 high-resolution airborne laser altimetry, *Geomorphology*, 57, 331-351,
626 [https://doi.org/10.1016/S0169-555X\(03\)00164-8](https://doi.org/10.1016/S0169-555X(03)00164-8), 2004.
- 627 29. Miao, F.S., Wu, Y.P., Li, L.W., Tang, H.M. and Li, Y.N.: Centrifuge model test on the retrogressive
628 landslide subjected to reservoir water level fluctuation, *Engineering geology*, 245: 169-179,
629 <https://doi.org/10.1016/j.enggeo.2018.08.016>, 2018.
- 630 30. Paronuzzi, P. and Bolla, A.: The prehistoric Vajont rockslide: an updated geological model,
631 *Geomorphology*, 169, 165-191, <https://doi.org/10.1016/j.geomorph.2012.04.021>, 2012.

- 632 31. Prokešová, R., Kardoš, M., Tábork, P., Medvedová, A., Stacke, V. and Chudy, F.: Kinematic
633 behaviour of a large earthflow defined by surface displacement monitoring, dem differencing, and
634 ERT imaging, *Geomorphology* 224, 86-101, <https://doi.org/10.1016/j.geomorph.2014.06.029>,
635 2014.
- 636 32. Qin, H.B.: The Mechanism of Landslide Influenced by Rainfall and Reservoir Water Level
637 Fluctuation and Renewed Criterion Research in Three-Gorges Reservoir, Dissertation, China
638 Three Gorges University, 2011(in Chinese).
- 639 33. Ren, F., Wu, X.L., Zhang, K.X. and Niu, R.Q.: Application of wavelet analysis and a particle
640 swarm-optimized support vector machine to predict the displacement of the Shuping landslide in
641 the Three Gorges, China, *Environmental earth sciences*, 73, 4791-4804,
642 <https://doi.org/10.1007/s12665-014-3764-x>, 2015.
- 643 34. Rinaldi, M. and Casagli, N.: Stability of streambanks formed in partially saturated soils and effects
644 of negative pore water pressures: the Sieve River (Italy), *Geomorphology*, 26, 253-277,
645 <https://doi.org/10.1007/s12665-014-3764-x>, 1999.
- 646 35. Rinaldi, M., Casagli, N., Dapporto, S. and Gargini, A.: Monitoring and modelling of pore water
647 pressure changes and riverbank stability during flow events, *Earth Surface Processes and
648 Landforms*, 29, 237-254, <https://doi.org/10.1002/esp.1042>, 2004.
- 649 36. Skempton, A.W.: Residual strength of clay in landslide, folded strata and the laboratory test,
650 *Géotechnique*, 35, 1-18, <https://doi.org/10.1680/geot.1985.35.1.3>, 1985.
- 651 37. Song, W.P.: The unsaturated seepage and stability analysis on slopes at river banks with the case of
652 Xicheng landslides in Yunyang. Dissertation, Chengdu University of Technology, 2011 (in

- 653 Chinese).
- 654 38. Song, K., Wang, F.W., Yi, Q.L. and Lu, S.Q.: Landslide deformation behavior influenced by water
655 level fluctuations of the Three Gorges Reservoir (China), *Engineering Geology*, 247, 58-68,
656 <https://doi.org/10.1016/j.enggeo.2018.10.020>, 2018.
- 657 39. Song, K., Yan, E.C., Zhang, G.D., Lu, S.Q. and Yi, Q.L.: Effect of hydraulic properties of soil and
658 fluctuation velocity of reservoir water on landslide stability, *Environmental earth sciences*, 74,
659 5319-5329, <https://doi.org/10.1007/s12665-015-4541-1>, 2015.
- 660 40. Sultan, H.A. and Seed, H.B.: Stability of sloping core earth dams, *Journal of the Soil Mechanics
661 and Foundations Division*, 93, 45-68, 1967.
- 662 41. Tan, F.L., Hu, X.L., Zhang, Y.M., He, C.C. and Zhang, H.: Study of progressive failure processes
663 and stabilities of different types of landslides, *Rock and Soil Mechanics*, 37, 597-606, 2016 (in
664 Chinese).
- 665 42. Tang, H.M., Li, C.D., Hu, X.L., Su, A.J., Wang, L.Q., Wu, Y.P., Criss, R.E., Xiong, C.R. and Li,
666 Y.A.: Evolution characteristics of the Huangtupo landslide based on in situ tunneling and
667 monitoring, *Landslides*, 12, 511-521, <https://doi.org/10.1007/s10346-014-0500-2>, 2015
- 668 43. Tang, H.M., Wasowski, J. and Juang, C.H.: Geohazards in the three Gorges Reservoir Area,
669 China - Lessons learned from decades of research, *Engineering Geology*, 261,
670 <https://doi.org/10.1016/j.enggeo.2019.105267>, 2019.
- 671 44. Terzaghi, K., Peck, R. B. and Mesri, G.: *Soil mechanics in engineering practice*, John Wiley &
672 Sons, 1996.
- 673 45. Wang, F.: Deformation prediction of Jiuxianping landslide in Yunyang Country based on

- 674 numerical simulation, Dissertation, Chengdu University of Technology, 2013 (in Chinese).
- 675 46. Wang, F., Zhang, Y., Wang, G., Peng, X., Huo, Z., Jin, W. and Zhu, C.: Deformation features of
676 Shuping landslide caused by water level changes in Three Gorges Reservoir area, China, Chinese
677 Journal of Rock Mechanics and Engineering, 26, 509-517, (in Chinese).
- 678 47. Wang, J.E., Xiang, W. and Lu, N.: Landsliding triggered by reservoir operation: a general
679 conceptual model with a case study at Three Gorges Reservoir, Acta Geotechnica, 9, 771-788,
680 <https://doi.org/10.1007/s11440-014-0315-2>, 2014.
- 681 48. Wang, H.L. and Xu, W.Y.: Stability of Liangshuijing landslide under variation water levels of
682 Three Gorges Reservoir, European Journal of Environmental and Civil Engineering, 17(sup1):
683 s158-s177, <https://doi.org/10.1080/19648189.2013.834592>, 2013.
- 684 49. Wen, T., Tang, H.M., Wang, Y.K., Lin, C.Y. and Xiong, C.R.: Landslide displacement prediction
685 using the GA-LSSVM model and time series analysis: a case study of Three Gorges Reservoir,
686 China, Natural Hazards and Earth System Sciences, 17, 2181-2198,
687 <https://doi.org/10.1002/esp.1042>, 2017.
- 688 50. Wu, Q., Tang, H.M., Ma, X.H., Wu, Y.P., Hu, X.L., Wang, L.Q., Criss, R.E., Yuan, Y. and Xu, Y. J.:
689 Identification of movement characteristics and causal factors of the Shuping landslide based on
690 monitored displacements, Bulletin of Engineering Geology and the Environment, 78, 2093-2106,
691 <https://doi.org/10.1007/s10064-018-1237-2>, 2019.
- 692 51. Xiao, S.R., Liu, D.F. and Hu, Z.Y.: Study on geomechanical model of Qianjiangping landslide,
693 Three Gorges Reservoir, Rock and Soil Mechanics, 28, 1459-1464, 2007 (in Chinese).
- 694 52. Yin, Y., Huang, B., Wang, W., Wei, Y., Ma, X., Ma, F. and Zhao, C.: Reservoir-induced landslides

695 and risk control in Three Gorges Project on Yangtze River, China, *Journal of Rock Mechanics and*
696 *Geotechnical Engineering*, 8, 577-595, <https://doi.org/10.1016/j.jrmge.2016.08.001>, 2016.

697 53. Zou, Z., Yan, J., Tang, H., Wang, S., Xiong, C. and Hu, X.: A shear constitutive model for
698 describing the full process of the deformation and failure of slip zone soil, *Engineering Geology*,
699 <https://doi.org/10.1016/j.enggeo.2020.105766>, 2020.